Analysis and mitigation of uncertainties in damage identification by modal-curvature based methods

Daniele Dessi [a,*], Fabio Passacantilli [a], Andrea Venturi [b]

[a] *Institute of Marine Engineering, National Research Council, Via di Vallerano 139, 00128 Rome, Italy*
[b] *Sapienza University of Rome, Department of Structural and Geotechnic Engineering, Via Eudossiana 18, 00184 Rome, Italy*

ARTICLE INFO

ABSTRACT

The objective of this paper is to address and reduce the uncertainties associated with measurement noise and discretization in damage identification methods based on modal curvature analysis. The experimental case study considers the local reduction in the bending stiffness of a slender beam under free-free and simply supported boundary conditions. First, the analysis of error sources and their propagation is theoretically set up. Second, the mitigation of uncertainties in damage localization is pursued using a two-stage approach based on multiple hypothesis testing relative to the normalized indices and the definition of a combined macro-index. Finally, the Monte Carlo method is exploited to obtain the statistical error distribution of the experimental damage position and severity predictions by randomizing the numerical displacement mode shapes with the identified noise. The present analysis allows us to find the optimal number of sensors that minimizes the combination of bias and truncation errors, to highlight how sensor spacing and data noise affect damage localization, and to determine the uncertainty bounds of the predicted damage severity. The two-stage approach, enhanced by selecting thresholds related to real noise levels and tuned on SHM objectives, appears to improve identification accuracy compared to the separate use of damage indices based on absolute confidence levels.

1. Introduction

The search for efficient and reliable non-destructive damage identification methods has become a common topic for several engineering sectors in recent decades. There is a tendency to combine (periodic) visual inspections with (continuous) analysis of data from sensors deployed in structural health monitoring (SHM) systems because the latter has become more widespread with the progressive introduction of artificial intelligence (AI) [1]. Therefore, some aspects that characterize damage identification methods seem to acquire increasing importance nowadays: (*i*) the derivation of damage criteria either from physical principles (physics-based methods) or from statistical and similarity features of data (data-driven methods), or even from combining both; (*ii*) the definition or not of a reference damage condition, i.e., methods with or without a baseline; (*iii*) the use of simulations to help recognize damage or interpret the results (transfer learning and hybrid analysis & modeling).

In a way similar to other methods relying on the analysis of vibration response, approaches based on curvature or strain energy assume that damage-induced variations in physical properties (mass, damping, stiffness, etc.) will cause detectable changes in modal properties (natural frequencies, modal damping, mode shapes, etc.). Pandey et al. [2] first demonstrated using FEM that absolute changes in modal curvature can be a good indicator of damage for beam-like structures by introducing the Mode Shape Curvature

---

method. Following this approach, several studies have further investigated the use of modal curvatures for damage assessment in different types of structures.

Most of the popular damage identification methods were initially developed in the context of one-dimensional beam-like and flat plate structures, such as the Gapped Smoothing Method (GSM) [3], the modal strain energy-based Damage Index Method by Stubbs et al. [4] and Cornwell et al. [5], the modal compliance-based method by Choi [6]-[7], the improved strain energy-based damage index by Kim [8] (including also frequency variation), and the Damage Severity Correction Factor by Fan and Qiao [9]. Stubbs et al. [10] instead proposed a general framework for damage assessment that accomplishes the Rytter's damage analysis levels [11]. The scheme underlying all these techniques lends itself to comparison with data analysis procedures developed more recently in the field of Machine Learning, as foreshadowed by Garcia et al. [12] in late nineties, who applied statistical pattern recognition to damage identification. In the proposed approach, physical world data (measurements) are first transformed into the so-called pattern space provided by modal quantities, and then dimensionality reduction simply turns into setting an upper bound on the number of considered modes. Then, nonlinear transformation is employed to obtain the feature space, which is divided into a finite number of clusters by a decision algorithm, one of them associated with damage. The latter step is analogous to setting index thresholds for damage detection in the techniques mentioned above.

The recent introduction of physics-based feature engineering, aimed at compensating for the scarcity of data with more problem-oriented features, continues to be of interest to these methods in the context of data-driven approaches. However, it is important to consider which points are susceptible to improvements that emerge from the analysis of the literature.

The development of new curvature-based methods has been progressively accompanied by limited comparisons with existing techniques. Dessi and Camerlengo [13] systematically compared several baseline and non-baseline methods in an error free-condition, focusing on their intrinsic capability of identifying damage. However, in only a few cases, the possibility of integrating the different methods has been considered. For instance, in Choi et al. [6] the average between two indices was introduced, but the new prediction was simply compared with those separately obtained without considering more sophisticated reasoning.

Over time, the way of judging the goodness of the methods has evolved. Initially, this was related to the ability to avoid false alarms. Subsequently, the need to minimize false negatives also emerged; however, an organic approach to assess performance is still lacking.

In the early days of curvature-based analysis, Farrar and Jauregui [14] pointed out the lack of precision of several methods for localizing the position of small damages. In general, the accuracy of damage identification is related to the amount of information available, that is, the number of sensors. This correlation has often been simplified by assuming that the damage covers the space between sensors. However, the possibility of the damage length being much smaller than the sensor spacing is common in applications. This has involved the adoption of curvature sub-sampling techniques to bring the problem back to the previous hypothesis, or introducing missing measurement points to obtain a denser grid with virtual sensing techniques (see [15]–[16]). In very few cases [6] the concept of equivalent stiffness reduction was introduced to parametrize the damage severity with respect to the measurement grid and to allow for further comparisons.

A descriptive mathematical model of the structure is often used to produce baseline data if this information is not available. However, the availability of such models has never been fully combined with on-field information to understand the propagation of noise from experimental data to the final indices and then to evaluate the prediction uncertainties. The relevance of addressing this aspect has been highlighted by Farrar and Jaregui [14], who proposed the development of procedures based on Monte Carlo or bootstrap methods to establish confidence limits on identified modal parameters. Limited to operational modal analysis, there have been several studies aimed at highlighting the effect of measurement errors on the modal parameters, *e.g.*, in stochastic subspace identification [17]-[18], and then the error propagation in quantities depending on the identification of mode shapes affected by uncertainties like, for instance, the Modal Assurance Criterion [19].

The present study aims to fill the gaps highlighted in the literature review in several directions: (*i*) improvement of damage predictions by combining several methods (Sections 2.2.1 and 2.2.2) into a multiple-hypothesis testing framework and by defining a macro-index (Section 2.3); (*ii*) definition of a threshold for the damage index related to detection target and noise level on input data (Section 4.3); (*iii*) analysis of the propagation of measurement noise up to the final index to assess the experimental uncertainties in damage prediction by using a Monte Carlo approach on noise-contaminated synthetic data (Section 4.3); (*iv*) a systematic analysis of numerical errors in the calculation of curvature and strain energy due to the finite number of nodes to allow for the determination of optimal sensor distance (Section 4.2) as best compromise between truncation (Section 3) and bias (Section 4) errors.

To provide a reference case for theoretical developments and successive experimental applications, a slender beam is considered under both free-free (FF) and simply supported (SS) boundary conditions (BCs) (Section 2.1). Free-free and simply supported BCs are representative of several applications of curvature-based methods in transportation systems, such as ships [20], or in civil structures, such as bridges [21]. The considered damage is a reduction in stiffness between the sensor nodes because this is a condition more frequently encountered in practical problems and requires employing displacement modes experimentally obtained from acceleration measurements. Moreover, this reduction is assumed to be uniform to allow the use of analytical solutions, thus speeding up calculations in the Monte Carlo analysis (Sections 5.3.2 and 5.4.2), and facilitating the verification of the exact correspondence with damage produced by milling in the laboratory beam. The methods developed by Cornwell et al. [5], Stubbs et al. [4], Choi et al. [6] and Kim and Stubbs [8] are considered herein (Section 2). The noise was preliminarily identified through a series of tests and allowed us to better evaluate the reliability of the prediction of damage severity.
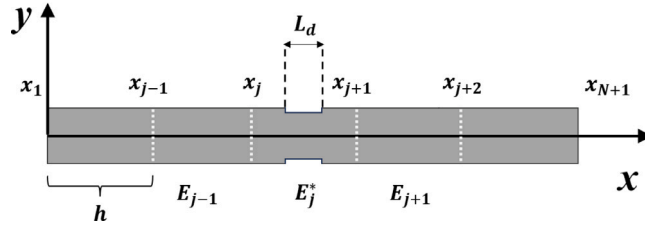
Fig. 1. Main definitions on the beam.

2. Methods based on curvature analysis with a baseline

2.1. Reference problem

The continuous Euler–Bernoulli beam shown in Fig. 1 is divided into N elements E_j by equally spaced nodes $x_j = (j-1)h$, with $j = 1, \ldots, N+1$ and h the sensor distance. The inner $N-1$ nodes define the positions where the sensors are placed physically or virtually. The damage is represented by a uniform stiffness reduction with length $L_d = |\xi_b - \xi_a|$, further assuming for the sake of simplicity that $I_d = [\bar{x}_j - L_d/2, \bar{x}_j + L_d/2] \subset E_j^*$, with $\bar{x}_j$ the element mid-point (in the following, all the variables relative to 'damaged' elements will be indicated with '*'). The displacement field $w(x,t)$ over the beam can be expressed by the modal superposition of the mode shapes $\phi^{(i)}(x)$ with $i = 1, \ldots, M$. Under the hypothesis of small displacements, the beam curvature is expressed as $\kappa(x,t) = w''(x,t) = \sum_{i=1}^{M} W^{(i)}(t)\,\kappa^{(i)}(x)$ where $\kappa^{(i)}(x) = \phi^{(i)\prime\prime}(x)$ is the ith modal curvature ($'$ indicates the space derivative), and $W^{(i)}(t)$ is the modal amplitude. The modal strain energy is defined as $U^{(i)} = \frac{1}{2}\int_0^L D(x)(\phi^{(i)\prime\prime}(x))^2\,dx$, where $D(x)$ denotes the sectional bending stiffness, which for the element E_j becomes $U_j^{(i)} = \frac{1}{2}\int_{x_j}^{x_{j+1}} D(x)(\phi^{(i)\prime\prime}(x))^2\,dx$. There exists a value $\bar{D}_j$ relative to element E_j, such that:

$$U_j^{(i)} = \frac{\bar{D}_j}{2} \int_{x_j}^{x_{j+1}} [\kappa^{(i)}(x)]^2\,dx = \bar{D}_j\,\gamma_j^{(i)}, \tag{1}$$

where $\gamma_j^{(i)}$, which is half the integral of the square of the modal curvature, represents a purely geometric quantity. The same consideration applies to the strain energy relative to the entire beam with $U^{(i)} = \bar{D}\,\gamma^{(i)}$.

2.2. Damage index definitions

Even if there is no common way of introducing the index definitions, there are two different forms of the damage indices: (*i*) a 'non-normalized' one, directly related to the stiffness reduction due to damage and so used to estimate the damage severity, and (*ii*) a 'normalized' one, obtained by Z-score normalization of the inverse of the 'non-normalized' index, aimed at localizing damage. Both forms of the indices are employed in this work, starting with the latter for the localization problem.

2.2.1. Methods related to strain energy

The methods proposed by Cornwell et al. [5] and Stubbs et al. [4] were based on similar assumptions. Cornwell et al. assumed that the ratio of local to global strain energies remains unchanged before and after damage, whereas for Stubbs et al. the local strain energies were supposed to be negligible compared to the global ones. Therefore, these methods provide similar expressions for the stiffness ratio, which is expressed by Cornwell et al. as:

$$\frac{D_j^*}{D_j} \simeq \frac{\gamma_j^{(i)}/\gamma^{(i)}}{\gamma_j^{(i)*}/\gamma^{(i)*}} \tag{2}$$

and by Stubbs et al. as:

$$\frac{D_j^*}{D_j} \simeq \frac{\gamma^{(i)*}\left(\gamma_j^{(i)} + \gamma^{(i)}\right)}{\gamma^{(i)}\left(\gamma_j^{(i)*} + \gamma^{(i)*}\right)} = \frac{1 + \gamma_j^{(i)}/\gamma^{(i)}}{1 + \gamma_j^{(i)*}/\gamma^{(i)*}} \tag{3}$$

The respective damage indices are usually expressed by summing over all the modes in both numerator and denominator, *i.e.*,

$$\beta_{\text{Co}} = \frac{\sum_{i=1}^{M} \gamma_j^{(i)}/\gamma^{(i)}}{\sum_{i=1}^{M} \gamma_j^{(i)*}/\gamma^{(i)*}} \tag{4}$$

$$\beta_{\text{St}} = \frac{\sum_{i=1}^{M} \gamma^{(i)*}\left(\gamma_j^{(i)} + \gamma^{(i)}\right)}{\sum_{i=1}^{M} \gamma^{(i)}\left(\gamma_j^{(i)*} + \gamma^{(i)*}\right)} \tag{5}$$

Kim and Stubbs [8] proposed a different formulation, by equating the change in system frequencies with the variation of strain energy in the damage element of a uniform beam, leading to the following expression of the stiffness ratio and the damage index:

$$
\frac{D_j^*}{\bar{D}} = \frac{\dfrac{\Delta\lambda_i}{\lambda_i}\gamma^{(i)} + \gamma_j^{(i)}}{\gamma_j^{(i)*}} \rightarrow \beta_{\mathrm{Ki}} = \frac{\sum_{i=1}^{M}\left(\dfrac{\Delta\lambda_i}{\lambda_i}\gamma^{(i)} + \gamma_j^{(i)}\right)}{\sum_{i=1}^{M}\gamma_j^{(i)*}},
\tag{6}
$$

where $\Delta\lambda_i = \lambda_i - \lambda_i^*$ is the variation in the ith pre- and post-damage eigenvalues of the observed structural system, and the term depending on the mass variation due to damage at the numerator has been neglected, consistent with the hypothesis stated above.

2.2.2. Method related to local analysis of curvature

A different family of methods relates the local reduction in stiffness to the comparison of curvature integrals. Choi et al. [6]-[7] proposed a damage index suitable to be applied to 1D and 2D structures using the concept of compliance. Its derivation is slightly different from that of the theories considered in this section. Choi et al. assumed that the load does not change after damage (this applies only to statically determinate structures) and, as a consequence, the distribution of the bending moment has to remain the same in both intact and damaged structures. After some math, the following expression for the stiffness reduction was obtained:

$$
\frac{D_j^*}{D_j} \simeq \frac{\displaystyle\int_{x_j}^{x_{j+1}} \kappa^{(i)}(x)\,dx}{\displaystyle\int_{x_j}^{x_{j+1}} \kappa^{(i)*}(x)\,dx}
\tag{7}
$$

The final index is often rearranged by considering the absolute value of and adding unity to both the numerator and the denominator. In addition, a separate summation of modal contributions is performed to increase the index sensitivity, thus obtaining:

$$
\beta_{\mathrm{Ch}} \simeq \frac{1 + \sum_{i=1}^{M}\left|\displaystyle\int_{x_j}^{x_{j+1}} \kappa^{(i)}(x)\,dx\right|}{1 + \sum_{i=1}^{M}\left|\displaystyle\int_{x_j}^{x_{j+1}} \kappa^{(i)*}(x)\,dx\right|}
\tag{8}
$$

2.2.3. Index normalization

Owing to the presence of noise in the curvature modes, the damage index is a random variable. It is a common practice for damage localization to introduce a Z-score normalized index, defined as

$$
\breve{\mathcal{B}}_{\mathrm{idx},j} = \frac{\breve{\beta}_{\mathrm{idx},j} - \bar{\breve{\beta}}_{\mathrm{idx}}}{\sigma_{\breve{\beta}_{\mathrm{idx}}}}
\tag{9}
$$

where 'idx' refers to a particular index (Cornwell, Stubbs, etc.), $\breve{\beta}_{\mathrm{idx},j} = 1/\beta_{\mathrm{idx},j}$ according to the definitions introduced in the previous sections, and $\bar{\breve{\beta}}_{\mathrm{idx}}$ and $\sigma_{\breve{\beta}_{\mathrm{idx}}}$ are the mean and standard deviation spanning all the beam elements, respectively. In the present study, damage detection (*i.e.*, existence and location) is based on the evaluation of $\breve{\mathcal{B}}_{\mathrm{idx},j}$, whereas the assessment of damage severity (*i.e.*, stiffness reduction) is based on $\beta_{\mathrm{idx},j}$.

Therefore, in an ideal error-free condition, positive values of $\breve{\mathcal{B}}_{\mathrm{idx},j}$ indicate a possible stiffness reduction, *i.e.*, $D_j^*/D_j < 1$, which can be further quantified via $\beta_{\mathrm{idx},j}$. The choice of confidence level for the random population $\breve{\beta}_{\mathrm{idx}}$ turns into different positive thresholds θ to decide whether an element is damaged ($\breve{\mathcal{B}}_{\mathrm{idx},j} \geq \theta$) or not ($\breve{\mathcal{B}}_{\mathrm{idx},j} < \theta$). There is no common choice for the threshold, which takes different values depending on the specific application. For instance, the threshold was set to 1 by Park et al. [22]), 1.5–1.625 by Choi et al. [6]–[23]) and 2 by Stubbs et al. [4]. Indeed, one of the scopes of this study is to provide new insights into the determination of the threshold based on the uncertainty analysis approach presented in Section 4.3.

2.3. Definition of a macro index

The various choices of the threshold are related to the different balances between false positives and false negatives that may be targeted. To mitigate uncertainties in damage identification, the proposed solution is the definition of a macro index based on the following two-stage process: (*i*) an element is potentially classified as damaged or not only if all the indices agree with each other (multiple hypothesis testing); (*ii*) the average of the (normalized) indices must exceed a given threshold, depending on the confidence level or on more sophisticated reasoning (see Sections 5 and 4.3). Therefore, it is assumed that element E_j is classified as:

- *Damaged,* if it satisfies all the conditions below:

    (a) *Agreement condition*: All the normalized index 'positively' agree, *i.e.*, $\forall\mathrm{idx}$, $\breve{\mathcal{B}}_{\mathrm{idx},j} > 0$ on the element E_j.
    (b) *Index-balancing condition*: The average value of the normalized indices, indicated as $\bar{\mathcal{B}}_{\mathrm{idx},j}$, overcomes a given threshold level θ.

- *Not Damaged,* if does not comply with at least one of the conditions (a) and (b).

3. Truncation error and sensitivity on sensor spacing

3.1. General formulation

Numerical evaluation of the local (element level) or global (domain level) integrals $\gamma_j^{(i)}$ (Eq. (1)) introduces truncation errors depending on the interpolatory quadrature formulas adopted. The same applies to the curvature integrals (Eq. (7)) but, for the sake of conciseness, theory is developed for $\gamma_j^{(i)}$ as a worse case. To achieve maximum spatial resolution for damage localization, the trapezoidal rule is typically used for the numerical evaluation of integrals delimited by grid nodes. Focusing on the jth element (Fig. 1), one has:

$$\gamma_j^{(i)} = \frac{1}{2} \int_{x_j}^{x_j+h} [\kappa^{(i)}(x)]^2 \, dx = \frac{h}{2} \left[\left(\kappa_j^{(i)} \right)^2 + \left(\kappa_{j+1}^{(i)} \right)^2 \right] - \frac{h^3}{12} (\kappa^{(i)\,2}(\xi_j))'' \tag{10}$$

where $\kappa_j^{(i)} = \kappa^{(i)}(x_j)$ and $\xi_j \in (x_j, x_{j+1})$ is a generic point of the element E_j of length h (see Hildebrand [24]). It is worth noting that the square of curvature $[\kappa^{(i)}(x)]^2$ does not admit the second-order spatial derivative at curvature nodal points, as they are turned into cusps; however, as it is continuous there, a previous error formula can be applied (see *e.g.*, Prenter [25]). Experimentally, the modal curvature value can be directly obtained by calibrating the strain gauges. If accelerometers are employed instead, a second-order central difference scheme must be used to evaluate the modal curvature $\kappa^{(i)}$ in node x_j:

$$\kappa_j^{(i)} = \tilde{\kappa}_j^{(i)} - (h^2/12)(\kappa_j^{(i)}(\tau_j))'', \tag{11}$$

where $\tilde{\kappa}_j^{(i)} = h^{-2}(\phi_{j-1}^{(i)} - 2\phi_j^{(i)} + \phi_{j+1}^{(i)})$ is the numerical approximation of $\kappa_j^{(i)}$, and the truncation error, depending on $(\phi^{(i)})^{IV}$, is expressed in terms of the modal curvature derivative, with $\tau_j \in (x_{j-1}, x_{j+1})$. By substituting Eq. (11), evaluated at both nodes x_j and x_{j+1}, into Eq. (10), one has:

$$\gamma_j^{(i)} = \tilde{\gamma}_j^{(i)} + R_{j,\text{trunc}}^{(i)} \tag{12}$$

where the approximation $\tilde{\gamma}_j^{(i)}$ and truncation error $R_{j,\text{trunc}}^{(i)}$ are expressed as follows:

$$\tilde{\gamma}_j^{(i)} = \frac{h}{2} \left[(\tilde{\kappa}_j^{(i)})^2 + (\tilde{\kappa}_{j+1}^{(i)})^2 \right] \tag{13}$$

$$R_{j,\text{trunc}}^{(i)} = -\frac{h^3}{12}(\kappa_j^{(i)}(\tau_j))'' \left(\tilde{\kappa}_j^{(i)} + \tilde{\kappa}_{j+1}^{(i)} \right) - \frac{h^3}{12}(\kappa^{(i)\,2}(\xi_j))'' + \frac{h^5}{144}[(\kappa_j^{(i)}(\tau_j))'']^2 \tag{14}$$

which implies that the final truncation error has two additional terms proportional to h^3 and h^5, owing to numerical differentiation. Recalling that the mode shapes are a linear combination of trigonometric and hyperbolic functions, such as $\phi^{(i)}(x) = A_1^{(i)} \sin(\beta_i x/L) + A_2^{(i)} \cos(\beta_i x/L) + A_3^{(i)} \sinh(\beta_i x/L) + A_4^{(i)} \cosh(\beta_i x/L))$, and the curvatures can be concisely expressed as $\kappa^{(i)}(x) = (\beta_i/L)^2 \varphi(x)$ with $\varphi(x) = -A_1^{(i)} \sin(\beta_i x/L) - A_2^{(i)} \cos(\beta_i x/L) + A_3^{(i)} \sinh(\beta_i x/L) + A_4^{(i)} \cosh(\beta_i x/L)$, Eq. (14) can be written as:

$$R_{j,\text{trunc}}^{(i)} = \frac{1}{12} \frac{\beta_i^6}{L^3} \left(\frac{h}{L} \right)^3 \left(-\phi_j(\tau_j) \left(\varphi_j^{(i)} + \varphi_{j+1}^{(i)} \right) - \psi(\xi_j) + \frac{\beta_i^2}{12} \left(\frac{h}{L} \right)^2 [\phi_j(\tau_j)]^2 \right), \tag{15}$$

where $\psi(x)$ is a nonlinear combination of trigonometric and hyperbolic functions such that $\kappa^{(i)\,2}(\xi_j))'' = (\beta_i/L)^6 \psi(\xi_j)$.

It is evident from Eq. (15) that, since typically $h/L = 1/N \ll 1$, the 5-th order term in h can be disregarded with respect to the leading 3-rd order terms. If the definite integral is extended to the entire beam length, the following is obtained:

$$\gamma^{(i)} = \frac{h}{2} \left[(\tilde{\kappa}_1^{(i)})^2 + 2 \sum_{j=2}^{N-1} (\tilde{\kappa}_j^{(i)})^2 + (\tilde{\kappa}_N^{(i)})^2 \right] + L \, h^2 \, f\left(\tilde{\kappa}_j^{(i)} \right) - \frac{L}{12} h^2 (\kappa^{(i)\,2}(\xi))'' + h.o.t. \tag{16}$$

where $\xi \in [0, L]$ and $f\left(\tilde{\kappa}_j^{(i)} \right)$ are functions of curvature estimates. It can be demonstrated in an analogous way that terms with powers equal to or higher than four can be disregarded.

3.2. Intact beam - Correlation between sensor spacing and errors

The sensitivity of the truncation error $|R_{j,\text{trunc}}^{(i)}|$ to the number of elements N, based on Eq. (14), gives an important indication about the suitability of the sensor layout. In Fig. 2, for the simply-supported BC, the truncation error $|R_{j,\text{trunc}}^{(i)}|$ is compared with the exact value of $\gamma^{(i)}$, analytically calculated and expressed with respect to the non-dimensional coordinate $\bar{x}_j/L$, mid-point of the element E_j, and the number N of elements E_j ito which the beam has been divided. The analytical integral is represented as a transparent surface with red mesh lines, whereas the error function is depicted as a surface with colors proportional to its z value. It is worth noting that the truncation error is always negligible for the first mode, but for the second mode, it is comparable to the exact $\gamma_j^{(i)}$ value as N approaches its lowest considered value ($N = 15$). The increase in errors with mode order is also evident for free-free BCs, with errors comparatively larger with respect to the simply supported case (see Fig. 3). The representation of the truncation error as a continuous function is useful for a direct comparison with the true value of $\gamma_j^{(i)}$, but does not consider that, inside each element E_j, the error terms must be evaluated at an unknown point. The upper limit of these terms is typically considered and varies with the element length, which depends on the overall number of beam divisions. Therefore, once N is set, the maximum value of $|R_{j,\text{trunc}}^{(i)}|$ in each element E_j is calculated. The discrete plots in Fig. 4 provide the first mode truncation error in
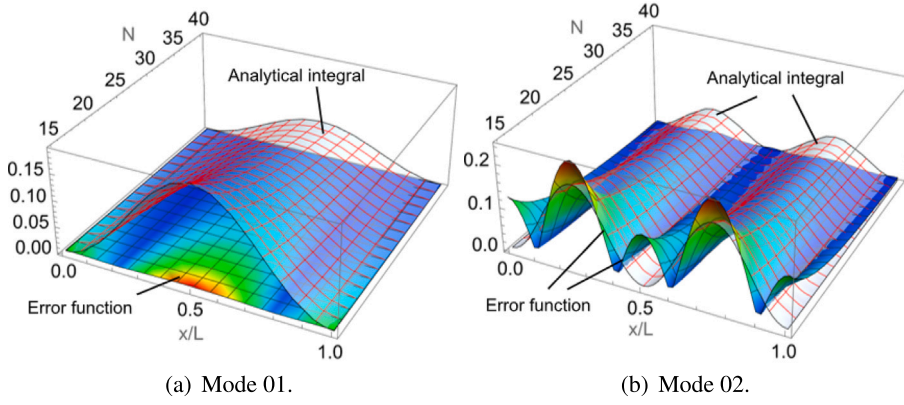
Fig. 2. Absolute truncation error function $|R^{(i)}_{j,\text{trunc}}|$ (colored surface) and analytical function of the integral $\gamma^{(i)}(\bar{x}_j/L, N)$ (red meshed surface) for simply-supported BCs (mode shapes with L_1 normalization). (For interpretation of the references to color in this figure legend, the reader is referred to the web version of this article.)
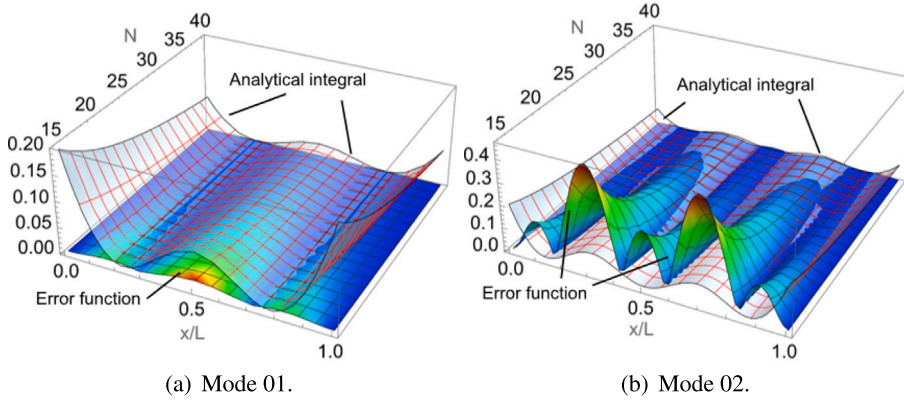

Fig. 3. Absolute truncation error function $|R^{(i)}_{j,\text{trunc}}|$ (colored surface) and analytical function of the integral $\gamma^{(i)}(\bar{x}_j/L, N)$ (red meshed surface) for free-free BCs (mode shapes with L_1 normalization). (For interpretation of the references to color in this figure legend, the reader is referred to the web version of this article.)

each element E_j for both SS and FF BCs. The error values are comparatively larger for the FF BCs and tend to increase significantly for $N < 20$.

By neglecting the 5-th order terms in Eq. (15) allows for finding a simple expression for the upper limit of $|R^{(i)}_{j,\text{trunc}}|$. Assuming simply-supported BCs, i.e., $\phi^{(i)} = A^{(i)}_1 \sin \beta_i x/L$, yields $|\phi_j(\tau_j)\left(\varphi^{(i)}_j + \varphi^{(i)}_{j+1}\right)| < 2$ and $|-\psi(\xi_j)| < 4$ and, consequently,

$$|R^{(i)}_{j,\text{trunc}}| < [A^{(i)}_1]^2 h^3 \frac{1}{2} \left(\frac{\beta_i}{L}\right)^6, \tag{17}$$

where β_i are nondimensional wave numbers, with $\beta_i = \beta^{SS}_i = i\pi$ for the simply supported beam. Eq. (17) holds also for FF BCs, with $\beta_i = \beta^{FF}_i = 4.7304, 7.38532, \ldots$ the solution of the characteristic beam equation (see [26]). However, its demonstration is rather involved, requiring writing the mode shape as $\phi^{(i)}(x) = A^{(i)}_1[\sin(\beta_i x/L) + \sinh(\beta_i x/L) + \Phi(\beta_i)(\cos(\beta_i x/L) + \cosh(\beta_i x/L))]$; then, it separately bounds the sum of trigonometric and hyperbolic functions, because $\Phi(\beta_i) = (\sin(\beta_i) - \sinh(\beta_i))/(\cos(\beta) - \cosh(\beta)) \simeq 1$ for $i = 1$ and it almost monotonically tends to unity as $\beta \to +\infty$. This upper bound for the absolute truncation error is higher for FF BCs because $\beta^{FF}_i > \beta^{SS}_i$ in agreement with the previous numerical results. From Eq. (17), a conservative estimation of the sensor grid spacing $h_{\min}$ satisfying the condition $|R^{(i)}_{j,\text{trunc}}| \leq \varepsilon$ can be obtained in both cases:

$$h_{\min} \leq [A^{(i)}]^{-2/3} \frac{(2\varepsilon)^{1/3}}{(\beta_i/L)^2} \tag{18}$$

From Eq. (18) it follows that, in general, $h^{SS}_{\min} > h^{FF}_{\min}$ since $\beta^{FF}_i > \beta^{SS}_i$. The latter consideration implies that in principle, dealing with SS BCs is less demanding in terms of the number of sensors.
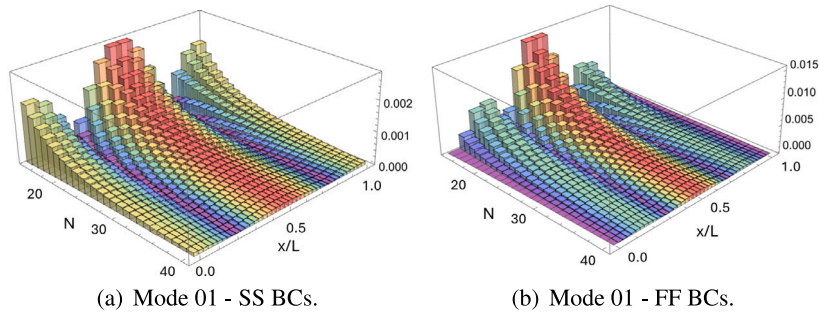
(a) Mode 01 - SS BCs. (b) Mode 01 - FF BCs.

Fig. 4. Element dependent upper bound of the absolute truncation error function $|R_{j,\text{trunc}}^{(i)}|$ (mode shapes with L_1 normalization).
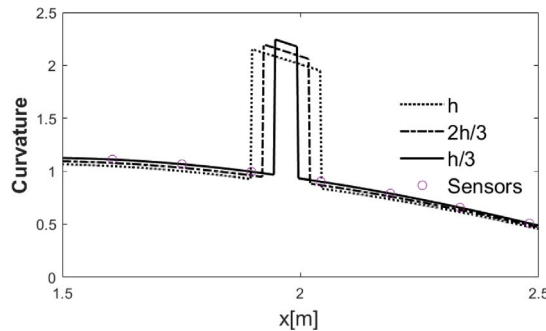

Fig. 5. Analytical modal curvature relative to the first mode with different damage lengths. The reference distance between the measurement points is set to $h = L/20$.

3.3. Damaged beam - Error sensitivity on damage length

Since the damage is modeled as a piecewise uniform reduction in stiffness along the portion $I = [\xi_a, \xi_b] \subset E_j^*$, the analytical curvature jumps as shown in Fig. 5, ruled by the relations $D \kappa^{(i)*}(\xi_a^-) = D^* \kappa^{(i)*}(\xi_a^+)$ and $D^* \kappa^{(i)*}(\xi_b^-) = D \kappa^{(i)*}(\xi_b^+)$, as reported in [13]. The two parameters describing the damage, *i.e.*, the stiffness reduction and its length, have two effects: (*i*) there is a local increment of modal curvature $\kappa^{(i)*}$ in the damaged portion and, consequently, of the integral and (*ii*), the modal curvature $\kappa^{(i)}(x)$ outside the damage is slightly decreased, with the effects increasingly fading the farther away, lowering the value of $\gamma_j^{(i)}$ with respect to the intact case. Because the modal curvature $\kappa^{(i)*}(x)$ does not admit derivatives at the damage edges, the previous expressions of the element truncation error can be applied only in the domain that does not contain the damaged element E_j^*, and one has only to rely on numerical computations to investigate the error sensitivity of the parameters.

It is interesting to focus on the dependence of the truncation error on the variation in relative damage length L_d/h. The damage length is symmetrically extended from the element mid-point $\bar{x}_c$. To illustrate some distinctive features of this dependency, we consider a specific case, that is, a beam divided into $N = 20$ elements and a damaged element E_c^* with $c = 14$. In Fig. 6, the truncation error relative to the first mode $i = 1$ is plotted along with $\gamma_c^{(1)*}$ and its approximation $\tilde{\gamma}_c^{(1)*}$. As expected, the numerical error in the damaged element increases in absolute value with damage length for $L_d/h < 1$, but the true value $\gamma_c^{(1)*}$ is underestimated. For $L_d/h \geq 1$, E_c^* remains fully damaged, but the error tends to decrease. Adjacent elements, such as E_{c-1}^*, have $\gamma_{c-1}^{(1)*}$ values similar to those of the damaged element as long as the damage length is small (see Fig. 7). As L_d increases, $\gamma_{c-1}^{(1)*}$ is overestimated. When the adjacent element begins to be partially damaged, the integral value $\gamma_{c-1}^{(1)*}$ increases, and the error decreases. The aforementioned considerations also apply to $j = c + 1$. In the case of free-free BCs, similar results are obtained.

4. Bias and random errors: propagation and evaluation of experimental uncertainty

Bias and random errors may heavily affect the determination of mode shapes and curvatures. Bias error is typically due to a not perfectly calibrated sensor or because the sensor is placed in a wrong position. Random errors originate from the combination of noise in measurements, limitations in signal acquisition, and numerical errors depending on the algorithm that extracts the displacement modes. Various hypotheses have been considered in the literature, and specific hypotheses are introduced here to account for bias and noise errors.
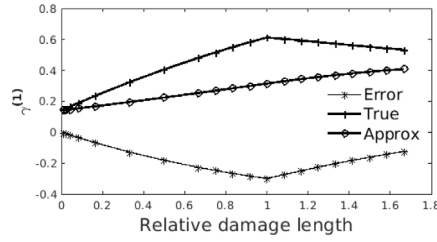
Fig. 6. Error sensitivity on the relative damage length L_d/h in evaluating $\gamma_c^{(1)*}$ in the damaged element (SS BCs).
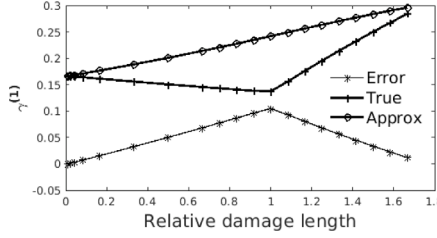

Fig. 7. Error sensitivity on the relative damage length L_d/h in evaluating $\gamma_{c-1}^{(1)*}$ in the damaged side element (SS BCs).

4.1. Bias error

It is reasonable to suppose that an error in the calibration of a single sensor at position j or an offset in its output will produce a bias error in the identified mode i at the neighboring points. Here, for the sake of simplicity, it is assumed that the mode shape $\phi^{(i)}(x)$ is subject to (bias) error only at node x_r, simply proportional to the modal amplitude, i.e., $\hat{\phi}_r^{(i)} = (1 + \eta_1^{(i)})\phi_r^{(i)} + \eta_0^{(i)}$ and $\hat{\phi}_j^{(i)} = \phi_j^{(i)}$ for $j \neq r$, then affecting the calculation of the strain energy in the elements E_{j-2}, E_{j-1}, E_j and E_{j+1}. By substituting the expression for the perturbed mode into Eq. (11), and the resulting expression into Eq. (10), one obtains for the square curvature integral relative to the generic element $E_j \equiv [x_j, x_{j+1}]$:

$$\hat{\gamma}_j^{(i)} = \gamma_j^{(i)} - \frac{\eta_0^{(i)} + \eta_1^{(i)}\phi_j^{(i)}}{h} \cdot \frac{2\phi_{j-1}^{(i)} - 5\phi_j^{(i)} + 4\phi_{j+1}^{(i)} - \phi_{j+1}^{(i)}}{h^2} + h.o.t. \tag{19}$$

where the higher-order terms (h.o.t.) refer to the powers of random parameters. By noting that the linear combination of the mode shape values, divided by h^2, is a 4-points, 2-nd order forward derivative, denoted as $\tilde{\kappa}_j^{(i)}$, it follows:

$$\hat{\gamma}_j^{(i)} = \gamma_j^{(i)} - \hat{\phi}_j^{(i)} \tilde{\kappa}_j^{(i)}/h + h.o.t. \tag{20}$$

which yields:

$$|R_{j,\text{bias}}^{(i)}| \simeq |\hat{\gamma}_j^{(i)} - \gamma_j^{(i)}| = \frac{|\hat{\phi}_j^{(i)}|}{h}|\tilde{\kappa}_j^{(i)}| \tag{21}$$

Next, a uniform upper limit for the proportionality coefficient $|\eta_1^{(i)}| < \eta_{\max}$ is set, and for simplicity, the constant part of the mode perturbation is set to zero, that is, $\eta_0^{(i)} = 0$. Thus, following the same considerations applied to the truncation error, we obtain the following bound for the bias error:

$$|R_{j,\text{bias}}^{(i)}| \leq [A^{(i)}]^2 \frac{\eta_{\max}}{h}\left(\frac{\beta_i}{L}\right)^2 \tag{22}$$

First, it is important to note that this expression also applies to strain energy errors relative to elements E_{j-2}, E_{j-1} and E_{j+1}, with minor modifications. In general, Eq. (21) points out that the error gets worse as h goes to zero, because errors on derivatives are comparatively more relevant than those related to integration. Moreover, the error is larger for points close to the maximum value of the displacement and curvature modes, which are the same for a simply supported beam.

4.2. Optimal step

While the bias error decreases with h, the truncation error increases with h. Therefore, there exists an optimum sensor distance h_{opt} that minimizes the sum of truncation and bias errors. Recalling Eqs. (17) and (22), it yields:

$$|R_{j,\text{bias}}^{(i)}| + |R_{j,\text{trunc}}^{(i)}| \leq [A^{(i)}]^2\left[\frac{\eta_{\max}}{h}\left(\frac{\beta_i}{L}\right)^2 + \frac{h^3}{2}\left(\frac{\beta_i}{L}\right)^6\right] = [A^{(i)}]^2\left(\frac{\beta_i}{L}\right)^2\left[\frac{\eta_j}{h} + \frac{h^3}{2}\left(\frac{\beta_i}{L}\right)^4\right] \tag{23}$$
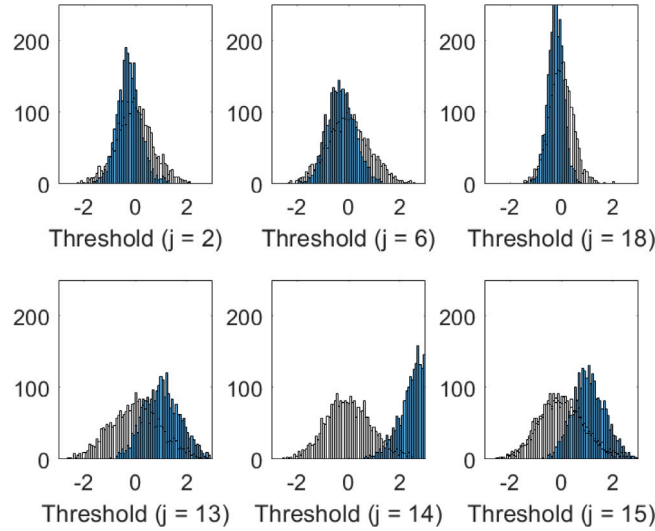
Fig. 8. Statistical distribution of the normalized Cornwell index (FF BCs, case A2 (Section 5), $\sigma_j^{(i)} = 0.001$). The distribution relative to damage case is represented in a darker color. (For interpretation of the references to color in this figure legend, the reader is referred to the web version of this article.)

The optimal step size which minimizes the above expression is:

$$h_{\text{opt}} = \left(2\,\eta_{\max}\right)^{1/4} \left(\frac{L}{\beta_i}\right) \tag{24}$$

or, passing to the optimal number of sensors,

$$N > L/h_{\text{opt}} = \beta_i \left(\frac{1}{2\,\eta_{\max}}\right)^{1/4}, \quad N \in \mathbb{N} \tag{25}$$

where N denotes the smallest integer greater than L/h_{opt}. Even in a weaker form, it is worth highlighting that the minimum number of sensors required to minimize the overall error is larger for free-free BCs because $\beta_i^{\text{FF}} > \beta_i^{\text{SS}}$.

4.3. Uncertainties due to random errors

Next, we assume that the 'perturbed' mode shape $\hat{\phi}_j^{(i)}$ due to random errors at the measurement and/or modal identification levels is given by:

$$\hat{\phi}_j^{(i)} = \phi_j^{(i)} + \eta_j^{(i)} \tag{26}$$

where $\eta_j^{(i)}$ is a normally distributed random variable with a mean equal to zero and a standard deviation $\hat{\sigma}_j^{(i)}$ to be determined from experiments relative to each node x_j. A simplified approach is based on modeling the dependence on a specific node by assuming the following linear expression for the variance:

$$\hat{\sigma}_j^{2(i)} = a_0^{(i)} + a_1^{(i)} \phi_j^{(i)} \tag{27}$$

and calculating the coefficients $a_0^{(i)}$ and $a_1^{(i)}$ using the least square method. If the determined coefficients are positive, it is equivalent to assuming the following expression of the perturbed modes $\hat{\phi}_j^{(i)} = (1 + \eta_1^{(i)})\phi_j^{(i)} + \eta_0^{(i)}$ with variances of the random variables $\eta_{1,2}^{(i)}$ given by the coefficients $a_{1,2}^{(i)}$. In the present study, the trivial expression for the noise introduced by Eq. (26) is used because linear fitting (Eq. (27)) may provide too conservative noise estimations.

In the present case, independently on using a linear fitting over the grid nodes or calculating in each node the variance, the mode shape coordinates are normally distributed variables (see *e.g.*, Fan and Qiao [9]-[27]). It is worth noting that, even in the case of modal displacement values uniformly distributed between $[-1, 1]$, as supposed by Choi et al. [28], the resulting statistical distribution of curvature values in each node after N_T trials, with N_T sufficiently large, tends to be Gaussian, following the central value theorem in an approximate way. In any case, the resulting damage indices are random variables that are not normally distributed owing to their nonlinearity with respect to curvatures. This aspect has not been sufficiently discussed in the past along with its consequences on statistical reasoning about the determination of damaged elements.

A Monte Carlo method is used to generate a random population of N_{rnd} damage scenarios, where each sample is constituted on one side by the set of noisy mode shapes of the intact structure and on the other side by the noisy mode shapes of the damaged structure. The exact mode shapes (intact or damaged) are contaminated with Gaussian noise with zero mean and a given variance (Eq. (26)). Analytical solutions are exploited to speed up the calculations [13]. For each damage scenario, non-normalized $\beta_{\text{idx},j}^{(i)}$
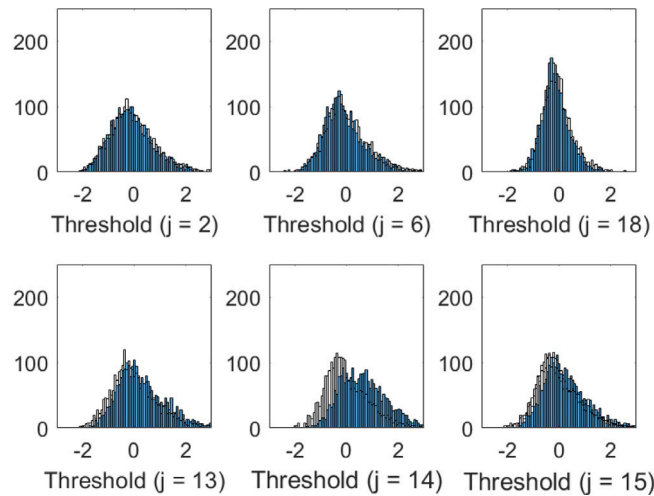
Fig. 9. Statistical distribution of the normalized Cornwell index (FF BCs, case A2 (Section 5), $\sigma_j^{(i)} = 0.005$). The distribution relative to damage case is represented in a darker color. (For interpretation of the references to color in this figure legend, the reader is referred to the web version of this article.)
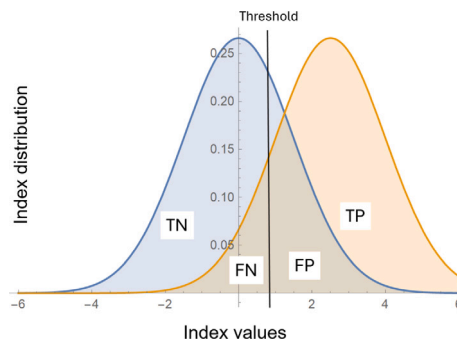

Fig. 10. Classification of normalized damage index predictions in case of intact and damaged elements based on definition of threshold.

and normalized $\check{\mathcal{B}}_{\mathrm{idx},j}^{(i)}$ damage indices are calculated, and finally a distribution of the damage index is obtained along the beam. Furthermore, to fully evaluate the capacity of separating the damage scenarios from the intact ones, which may appear erroneously as damaged, a second random population of N_{rnd} samples is built. Each sample is obtained by associating the noisy intact mode shapes with another set, randomly generated as well, of noisy intact mode shapes. This second population is called 'neutral.'

For conciseness, only the Cornwell theory is applied to the model of the experimentally tested beam. In Fig. 8, assuming for all the nodes and modes a standard deviation $\sigma_i^{(i)} = 10^{-3}$, imposing a localized stiffness reduction equal to the case A2 (see Section 5) under FF BCs, the statistical distribution of the normalized Cornwell index $\check{\mathcal{B}}_{\mathrm{idx},j}^{(i)}$ is shown for several elements of the 'damaged' population (dark bars), along with the statistical distribution relative to the 'neutral' population (white bars). It is worth noting that the Cornwell index is similarly distributed for elements not affected by damage, such as elements E_2, E_6 or E_{18}. However, for the damaged element E_{14} and the adjacent ones E_{13} and E_{15}, the index distribution is globally shifted to higher values. Thus, for element E_{14}, it is possible to choose a threshold level that separates the intact and damaged classes quite well. If the same analysis is repeated with a higher noise level, with variance, $\sigma_i^{(i)} = 5 \cdot 10^{-3}$ (see Fig. 9), it is more difficult to separate the intact and damaged index distributions. Setting a threshold to classify an element as damaged provides a certain number of true negatives (TN) and false negatives (FN) for undamaged elements, and true positives (TP) and false positives (FP) for damaged elements, as depicted in Fig. 10. It is clear that moving the threshold backward and forward as shown in Fig. 9, spanning the index range, affects the accuracy in classifying the beam elements. The question then is how to rationally tune this threshold, minimizing, for instance, the number of false alarms (FP) or the number of undetected damages (FN). In Figs. 11 and 12, the Receiver Operating Characteristics (ROC) curves are shown for two different noise levels ($\sigma_j^{(i)} = 0.001, 0.005$), parameterized on the threshold value θ. The x-axis represents the False Positive Rate ($FPR = FP/(FP + TN)$) and y-axis represents the True Positive Rate ($TPR = TP/(TP + FN)$). The ROC is compared with a diagonal line representing the random classifier. There is a point along the ROC that is the farthest from the random classifier, which is relative to the optimal threshold θ_{opt} which better separates the 'neutral' and 'damaged' classes and provides the highest Accuracy (ACC), defined as:

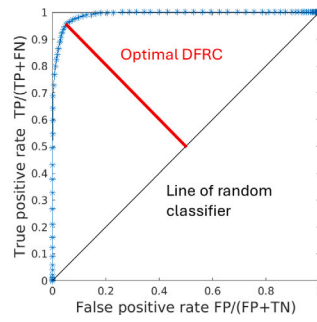$$ACC = \frac{TP + TN}{TP + FN + TN + FP} \tag{28}$$

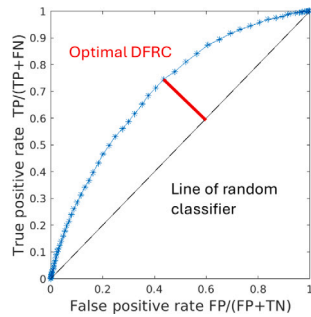**Fig. 11.** ROC of the Cornwell index ($\sigma_j^{(i)} = 0.001$, FF BCs, damage case A2).

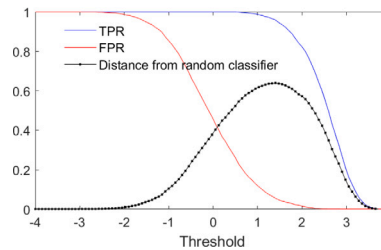**Fig. 12.** ROC of the Cornwell index ($\sigma_j^{(i)} = 0.005$, FF BCs, damage case A2).

Fig. 13. TPR, FPR and Distance from random classifier of the Cornwell index ($\sigma_j^{(i)} = 0.001$, FF BCs, damage case A2).

The presence of an optimal threshold point, θ_{opt} is shown in Figs. 13 and 14, where the TPR, FPR and distance-from-random-classifier (DFRC) are plotted with respect to the threshold. It should be noted that, while it is easy to identify an optimal threshold at $\theta_{\mathrm{opt}} \simeq 1.4$ (*i.e.*, high TPR and low FPR) for low noise values, for high noise values, this point is less meaningful and the peak value falls back close to 0. This does not mean that classification produces random results, but that there is no way to achieve a good compromise in terms of the maximization of the TPR and minimization of the FPR. While it is evident that the optimal threshold depends on the noise level, it does not depend significantly on the position of the damage along the beam. In Fig. 15 the optimal threshold, calculated for different positions of the damage, varies in the range [1.2 − 1.5] for the case $\sigma_j^{(i)} = 0.001$.

The previous analysis can be repeated for the non-normalized damage index $\beta_{\mathrm{idx},j}^{(i)}$. In this case, however, the scope is to calculate the uncertainty related to the experimental prediction of the damage severity. To illustrate this concept, we eliminate the assumption of single-beam damage. Figs. 16 and 17 show the Cornwell index distribution $\beta_{\mathrm{idx},j}^{(i)}$ across the beam in terms of mean values and uncertainties bounds for different distances between two damaged elements, one fixed in the middle of element E_{14}, and the other getting different positions along the beam. The stiffness reduction associated with both positions is the same as previously assumed (experimental case A2 with FF BCs, see Table 2). It can be observed that when the damages are far away (Figs. 16(a) and 16(b)), the index variations are localized around the damaged element, and there is no interference of one on the other. This perturbation of the index value in the neighboring elements due to the use of finite differences will be further considered and explained in Section 5.2. On the other hand, when damage occurs to the neighboring elements (Fig. 17(a)), the index variations tends to mix together and to heavily affect the intact value in the side element, becoming not easily distinguishable from a true damaged one. With this unique exception, the curvature-based indices used in this study are able to identify multiple damages to the structure (see also Fig. 17(b)). In the extreme case of uniformly distributed damage across the beam, the curvature-based indices tend to become
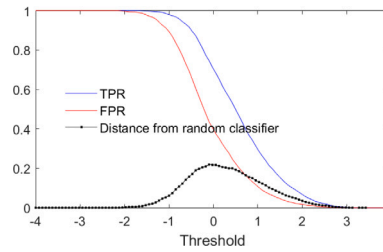
Fig. 14. TPR, FPR and Distance from random classifier of the Cornwell index ($\sigma_j^{(i)} = 0.005$, FF BCs, damage case A2).
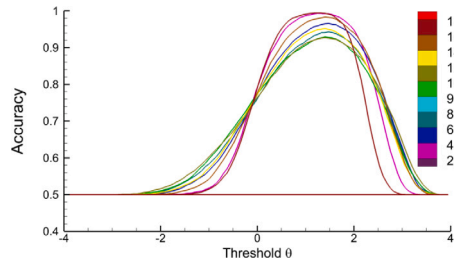

Fig. 15. Accuracy plot with respect to threshold for different damage positions ($\sigma_j^{(i)} = 0.001$, FF BCs, damage case A2).

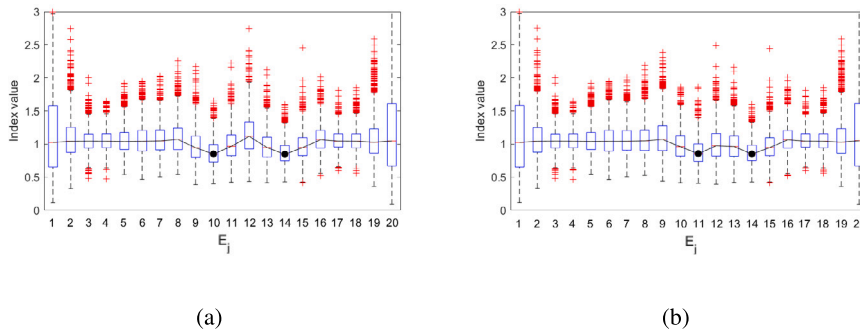(a)   (b)

Fig. 16. Cornwell index distribution and uncertainty quantification for different scenarios of two damages on the beam. The damaged elements are indicated by a black circle on the index value for the damaged elements.

Table 1
Geometrical and physical characteristics of the intact beam.

Length	Width	Height	Thickness	Young modulus	Density
2.918 m	0.080 m	0.040 m	0.004 m	$69 \cdot 10^9$ Pa	2.677 kg/m^3

insensitive to continuous damage because, by definition, the local curvature variations are not affected by a uniformly distributed stiffness reduction.

5. Experimental damage identification for the beam

5.1. Case-study and experimental setup

The physical system under consideration is a hollow rectangular section aluminum beam, the characteristics of which are listed in Table 1.

Free-free BC (Fig. 18(b)), achieved by means of four soft springs, has the advantage of easy reproducibility test after test. The simply supported layout (Fig. 18(a)) requires some care in ensuring that small changes in the forces and/or moments exerted by the constraint mechanism do not affect the modal parameters more then the stiffness variation due to damage.

As highlighted in Section 2.1, the beam cross section is uniformly modified in a beam portion of length $L_d = 0.05$ m to represent a local damage, centered at the element mid-point $\bar{x}_j$. Thickness reduction. equal to 0.002 m is obtained by milling a single (top)
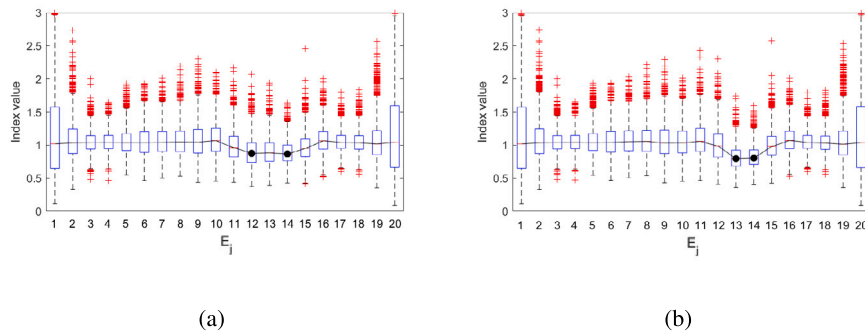
(a)

(b)

Fig. 17. Cornwell index distribution and uncertainty quantification for different scenarios of two damages on the beam. The damaged elements are indicated by a black circle on the index value for the damaged elements.
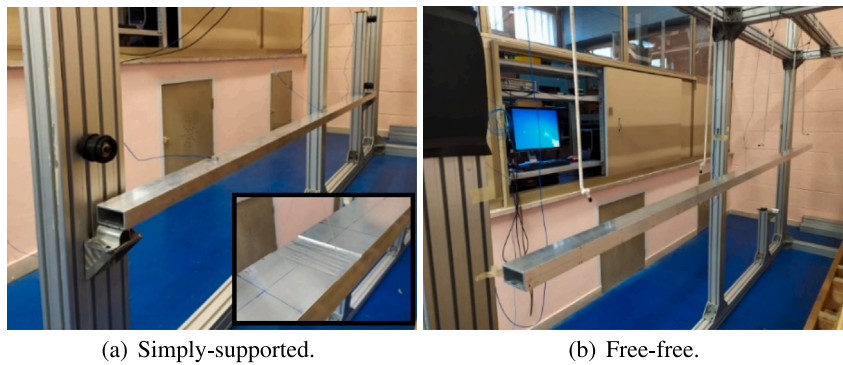

(a) Simply-supported.

(b) Free-free.

Fig. 18. Physical model and experimental set-up for damage identification.

Table 2
Intact and damaged beam layouts.

Damage case	$\bar{x}_{14}$	Thinned faces	Local Stiffness ratio	Mean Stiff. ratio in E_{14}	$\bar{x}_{04}$	Thinned faces	Mean Stiff. ratio in E_{04}
R0	N/A	0	1	1	N/A	0	1
A1	1.985 m	1	0.721	0.907	N/A	0	1
A2	1.985 m	4	0.43	0.841	N/A	0	1
B1	1.985 m	4	0.43	0.841	0.511 m	1	0.907
B2	1.985 m	4	0.43	0.841	0.511 m	4	0.841

face of the beam (see the bottom-right framed image in Fig. 18(a)) or all the beam sides. The milling process was performed in a dedicated facility to ensure safe arrangement and minimization of undesired residual deformations. The damage position and severity are reported and labeled in Table 2.

The beam was divided into $N = 20$ elements ($h = L/N = 0.1459$ m) by setting equally spaced $N_{exp} = 19$ degrees of freedom (DoFs) for the Roving Hammer Technique (RHT), which uses two mono-axial accelerometers PCB333B32 in fixed positions and an instrumented hammer (see Table 3). The sensor signals were acquired using the LMS SCADAS SCM05 acquisition system with 24 VB8 channels controlled by Siemens LMS Test. Lab 19 software. The LMS SCADAS system has up to 204.8 kHz sampling rate per channel and throughput of up to 14 MSamples/s with a 150-dB dynamic range, with 24-bit delta-sigma ADC technology. Owing to the use of finite differences in the acceleration signals, modal curvatures are available only at the inner points $N_{exp} - 2$ of the sensor grid. This implies that the modal strain energy or curvature integrals can be calculated only for $N - 4$ elements. Therefore, using ideal BCs, the modal curvature values are recovered in the missing points. This is performed directly at the beam edges imposing $\phi_1''^{(i)} = \phi_{N+1}''^{(i)} = 0$ for both the SS and FF BCs. In adjacent points x_2 and x_N, the calculation of curvature requires the availability of the displacement value at the beam edges to apply the finite difference formula. The displacement value is directly provided by ideal SS BCs ($\phi_1^{(i)} = \phi_{N+1}^{(i)} = 0$) and, in the case of FF BCs, by imposing a cubic polynomial passage through experimental points at nodes x_1 and x_2 (or x_{N-1} and x_N) and conditions on derivatives at the beam edges, $i.e.,$, $\phi_1''^{(i)} = \phi_1'''^{(i)} = 0$ (or $\phi_{N+1}''^{(i)} = \phi_{N+1}'''^{(i)} = 0$)

Table 3
Accelerometer characteristics.

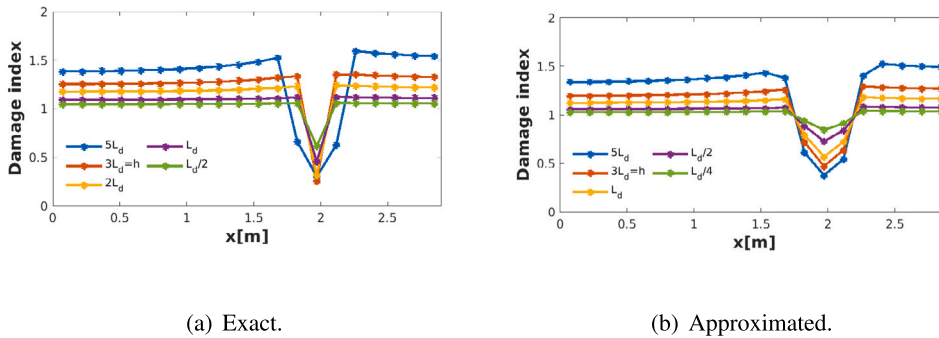| Sensitivity	Resolution	Frequency range	Meas. range
$100\,\mathrm{m\,V/g}$	$0.0001\,\mathrm{g\,rms}$	$0.3 - 5000\,\mathrm{Hz}$	$\pm 50\,\mathrm{g\,pk}$

(a) Exact.   (b) Approximated.

Fig. 19. Exact and approximated damage index based on analytical mode calculation for simply-supported boundary conditions.
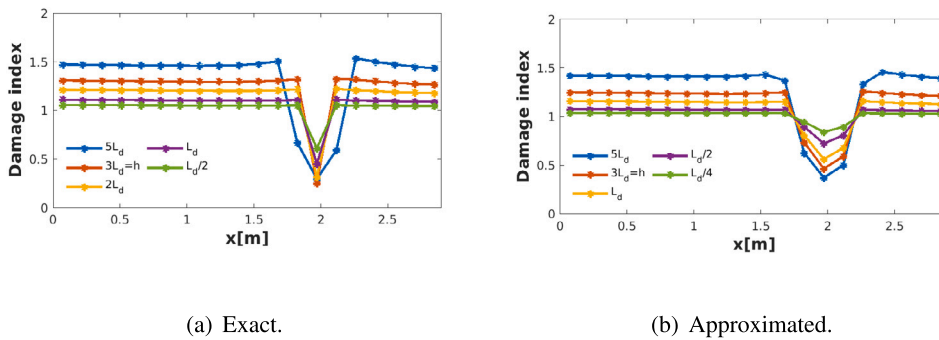
(a) Exact.   (b) Approximated.

Fig. 20. Exact and approximated damage index based on analytical mode calculation for free-free boundary conditions.

from ideal BCs. All the indices evaluated in the following subsections, both in normalized or non-normalized form, utilize $M = 5$ modes.

5.2. Errors due to the sensor layout

Prior to the analysis of the experimental data, it is important to understand the implications of the sensor layout on the damage identification results. The first aspect concerns the calculation of curvature integrals from the displacement modes, identified via the measurement of accelerations. The use of finite differences in the curvature calculation (Eq. (11)) and trapezoidal rule (Eq. (12)) allows for sensing damage between experimental nodes but also yields a phenomenon sometimes named as precision leakage, but here referred as *damage position spill* (DPS) for the sake of clarity. Thus, even if the damage length is less than the accelerometer distance, the adjacent elements appear to be damaged in the analysis. To explain the DPS, a representative sensitivity analysis of the non-normalized Cornwell index on the damage length is carried out assuming the stiffness reduction A2 in the element E_{14} as a reference case. The Cornwell index, selected because of its simply dependence on $\gamma_j^{(i)}$ and $\gamma_j^{(i)*}$, is calculated in two ways, called 'exact' and 'approximated.' In the 'exact' form, the true values of the nodal curvatures and element integrals are available. In the 'approximated' form, the index is built by sampling the analytical modal shapes in the experimental dofs x_j and then applying the differentiation and quadrature formulas, as it occurs in processing experimental data. In Figs. 19(a) and 20(a), the 'exact' Cornwell index is plotted along the beam. There is no damage position spill because the index curve has a minimum of less than unity (damage existence) only in the damaged element E_{14} as long as $L_d \leq h$. The 'approximated' index (Figs. 19(b) and 20(b)) shows instead values less than unity also in nearby elements. It is worth noting that if the true damage extends to the adjacent elements ($Ld > h$), no position spill is present and so the discrepancy between 'exact' and 'approximated' indices are less evident. This fact must be taken into account when examining the correctness of damage identification results because adjacent elements may determine a 1-element shift in the damage location but point to the existence of the same physical damage.

Table 4

Optimal number of elements N and sensor spacing h for two different values of the assumed bias-error upper limit $\eta_{\max}$ on displacement modes.

Mode	$\eta_{\max}$	h_{opt}^{SS}	N^{SS}	h_{opt}^{FF}	N^{FF}	Mode	$\eta_{\max}$	h_{opt}^{SS}	N^{SS}	h_{opt}^{FF}	N^{FF}
1	0.01	0.3494	9	0.2320	13	1	0.02	0.4145	8	0.2887	11
2	0.01	0.1747	17	0.1397	21	2	0.02	0.2077	15	0.1739	18
3	0.01	0.1165	26	0.0998	30	3	0.02	0.1385	22	0.1242	25
4	0.01	0.0873	34	0.0776	38	4	0.02	0.1039	29	0.0966	32
5	0.01	0.0699	42	0.0635	46	5	0.02	0.0831	36	0.0790	39

Table 5

Frequency related to the identified vibration modes relative to different configurations for FF BCs.

Damage case	1st mode [Hz]	2nd mode [Hz]	3rd mode [Hz]	4th mode [Hz]	5th mode [Hz]
R0	33.43	91.88	178.46	291.35	428.56
A1	33.34	91.28	178.36	290.85	428.51
A2	33.01	90.50	178.25	290.30	424.70
B1	32.54	88.87	175.03	287.48	419.50
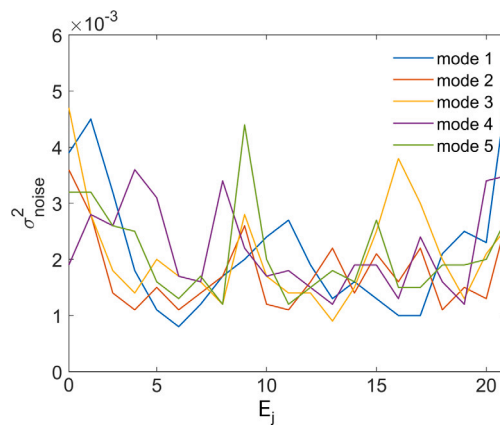
Fig. 21. Distribution of standard deviations relative to mode identification with RHT along the experimental nodes for FF BCs and intact condition.

Differences between the 'exact' and 'approximated' indices exist also in the value of the minimum, directly linked to the equivalent stiffness ratio $\bar{D}_{14}^*$. However, these differences are less than expected from the analysis of truncation errors on $\gamma_j^{(i)*}$ and $\gamma_j^{(i)}$ because the latter are partially filtered in the calculation of $\gamma_j^{(i)*}/\gamma_j^{(i)}$ if they have the same sign.

The second aspect is related to sensor grid density. In Section 3 it has been quantitatively shown that the truncation error reduces as more experimental dofs are available, that is, a lower distance between (virtual) sensors. A denser experimental grid also results in a more precise localization of damage (apart from the considerations made previously). In contrast, Table 4 obtained by applying Eqs. (24) and (25) to the present problem, reports the optimal number of sensors which minimizes the sum of bias and truncation errors in the evaluation of $\gamma_j^{(i)}$ (an optimal point exists because of opposite dependency on h). The optimal number of sensors increases with the mode order but decreases with the bias error $\eta_{\max}$ (this does not imply that the related error diminishes as well). It is also worth noting that the optimal number of sensors as the mode order increases tends to be similar for the SS and FF BCs. This implies that the sensor spacing in the laboratory experiments, with $N = 20$, is a good compromise between the different optimal choices related to the mode order for a bias error level $\eta_{\max} = 0.02$, while it is slightly less than that required for $\eta_{\max} = 0.02$.

5.3. Free-free boundary conditions

5.3.1. Damage existence and localization

The first chance of receiving a warning about the possible existence of damage may simply come from the analysis of modal frequencies. In Table 5 the variation in the natural frequency relative to the first five vibration modes is reported for each damage case. As expected, the frequencies generally tend to decrease as the stiffness decreased. However, because the average stiffness variation, *i.e.*, the local stiffness reduction spread over the beam, is in the range $0.005\% - 0.01\%$ (low/high stiffness reduction), there are few opportunities to assess the existence of damage uniquely by considering the frequency variation. The experimental noise on the identified mode shapes, whose standard deviation distribution is shown in Fig. 21 for each mode, determine curvature modes rather irregular (Fig. 22), regardless their nature (intact or damaged), even turning positive curvatures into negative and vice-versa,
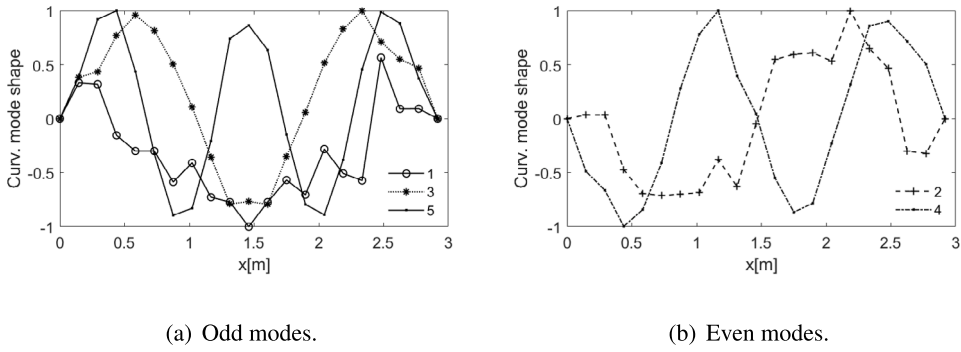
(a) Odd modes.

(b) Even modes.

Fig. 22. Curvature mode shapes for configuration R0 with free-free BCs.
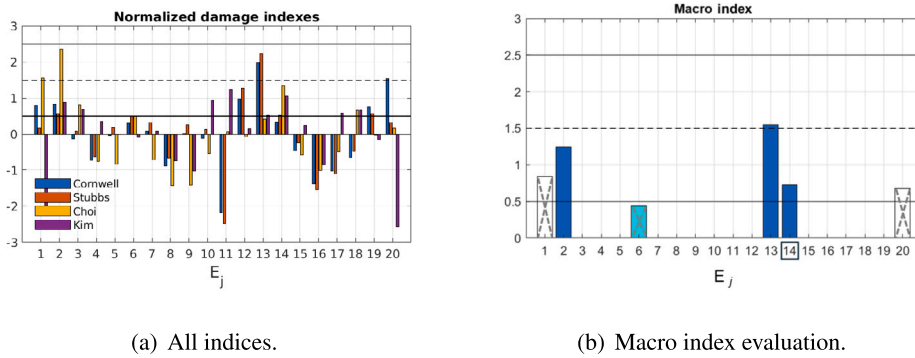

(a) All indices.

(b) Macro index evaluation.

Fig. 23. Normalized damage indices for scenario R0(intact)-A1(damaged) under FF BCs. Element-weighted stiffness ratio is $\bar{D}^*_{14} = 0.907$. (For interpretation of the references to color in this figure legend, the reader is referred to the web version of this article.)
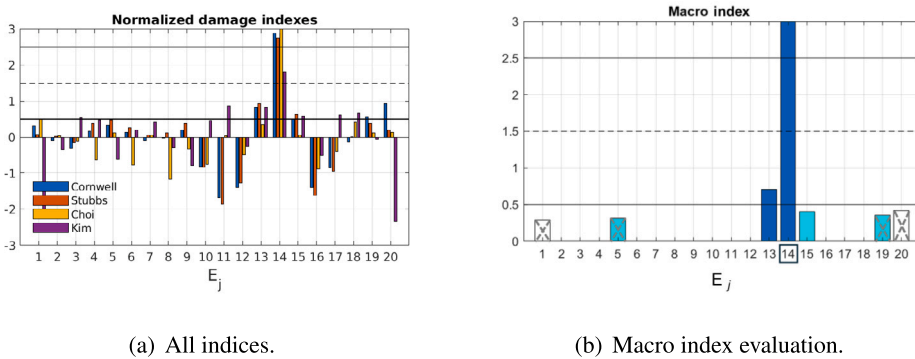

(a) All indices.

(b) Macro index evaluation.

Fig. 24. Normalized damage indices for scenario R0(intact)-A2(damaged) under FF BCs. Element-weighted stiffness ratio is $\bar{D}^*_{14} = 0.841$.

especially for low order modes. The noise on the curvature modes propagates to the normalized damage indices, introducing both false positives and false negatives, and enhancing the possibility of disagreement between the indices, as shown, for instance, in Fig. 23(a), relative to the damage scenario R0-A1.

To highlight the concordance between the indices, a second diagram is introduced to show the macro-index defined in Section 2.3. The bars in Fig. 23(b) indicate the positive agreement between the indices in the generic element E_j and their value is set equal to the macro-index $\bar{\mathcal{B}}_{\text{idx},j}$, here defined as the mean of the normalized Cornwell, Stubbs and Choi indices. Damage scenario R0-A1 in Fig. 23 considers a sectional stiffness ratio $D^*/D = 0.721$ corresponding to an element-weighted ratio equal to $\bar{D}^*_{14} = 0.907$. For clarity, the damage position is highlighted by placing a box around the number relative to the damaged elements. The prediction of damage at the edge elements is not considered meaningful because the index calculation is strongly affected by the hypotheses relative to the displacement and curvature at the end points (x_1 and x_{21}); for this reason, the corresponding bars are colored white.
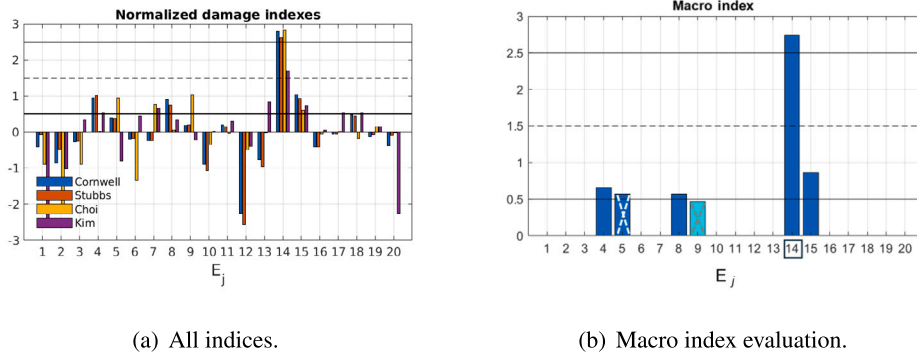
(a) All indices.

(b) Macro index evaluation.

Fig. 25. Normalized damage indices for scenario A1(intact)-A2(damaged) under FF BCs. Element-weighted stiffness ratio is $\bar{D}_{14}^* = 0.86$.

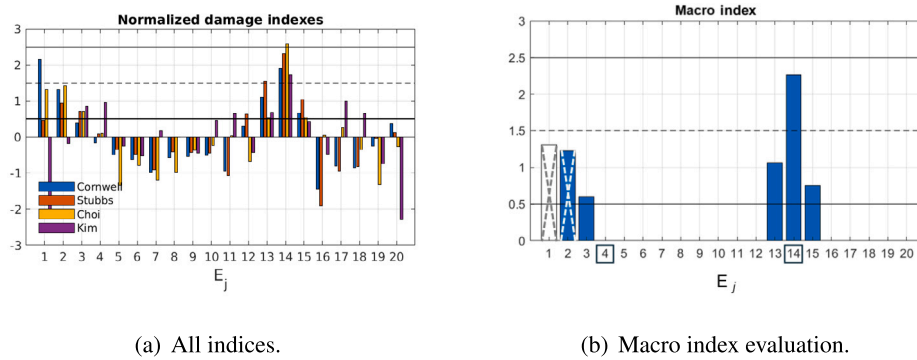(a) All indices.

(b) Macro index evaluation.

Fig. 26. Normalized damage indices for scenario R0(intact)-B1(damaged) under FF BCs. Element-weighted stiffness ratios are $\bar{D}_{14}^* = 0.841$ and $\bar{D}_{04}^* = 0.907$.
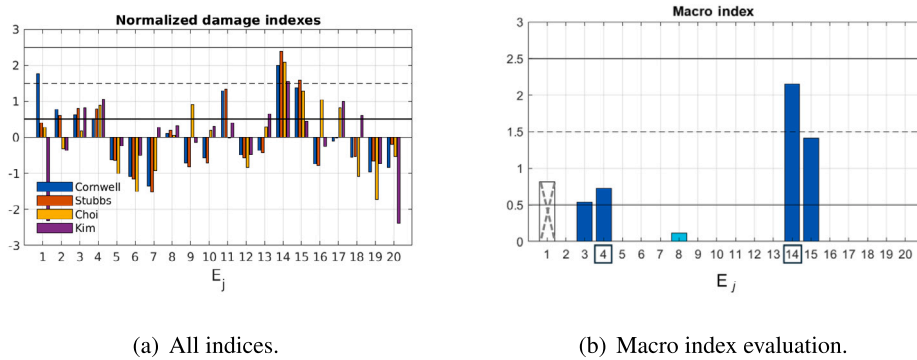

(a) All indices.

(b) Macro index evaluation.

Fig. 27. Normalized damage indices for scenario A1(intact)-B1(damaged) under FF BCs. Element-weighted stiffness ratios are $\bar{D}_{14}^* = 0.86$ and $\bar{D}_{04}^* = 0.907$.

The macro-index exploits agreement/disagreement analysis to lower the possibility of false positives and, consequently, relaxes the need for high thresholds. In any case, macro-index values less than 0.5 are related to rather small confidence levels and therefore cannot be representative of damage (colored cyan). Nevertheless, adding the Kim and Stubbs index allows for 'cleaning' damage predictions, *i.e.*, further reducing the false positives. Therefore, a cross is drawn on the bars if the Kim and Stubbs index disagrees with other indices. This means that the inclusion of the last index has led to disregard the positive macro-index value in the diagram.

Similar results can be obtained if the damage is increased by setting $D^*/D = 0.43$, with an element-weighted stiffness ratio $\bar{D}_{14}^* = 0.81$ (comparison between cases R0 and A2, see Fig. 24), or for the intermediate damage scenario obtained by comparing cases A1 and A2, providing an element-weighted stiffness ratio equal to 0.865 (Fig. 25). It is also interesting to repeat the analysis by introducing damage on element E_4 (case B1) and comparing it with the intact condition R0, as shown in Fig. 26. While damage on the element E_{14} is correctly identified, no damage is found on element E_4. False positives appear on elements E_2 and E_3: the
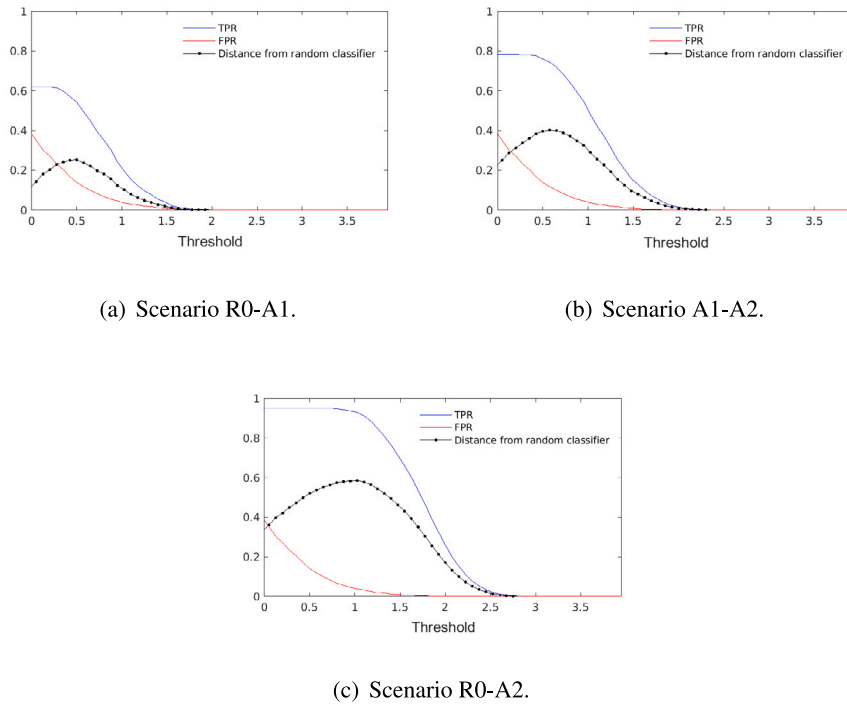
(a) Scenario R0-A1.

(b) Scenario A1-A2.

(c) Scenario R0-A2.

Fig. 28. Dependency of TPR, FPR and distance from random classifier on the threshold value θ (FF BCs).

Table 6
Data from the confusion matrix calculated on the optimal threshold value (FF BCs). In case of two-point damage, the first threshold is applied to damage in position $j_d = 14$, the second to position $j_d = 4$. The lowest of the two threshold is applied for all the other points.

Scenario	θ_{opt}	TP	FN	FP	TN	ACC	DSE	ACC+
R0-A1	0.5	1	0	2	15	88.8%	1	94.4%
A1-A2	0.65	1	0	1	16	94.4%	1	100%
R0-A2	1	1	0	0	17	100%	0	100%
R0-B1	1/0.5	1	1	2	14	83.3%	2	94.4%
A1-B1	0.65/0.5	2	0	2	14	88.8%	2	100.0%

first one can be eliminated including the Kim and Stubbs index in the agreement condition, while the second is related to DPS occurrence. Accuracy in damage identification improves if A1 condition is taken as reference for the intact condition (Fig. 27).

As outlined before, to classify the elements as damaged or intact, index thresholds are based on a sensitivity analysis of the TPR, FPR and Accuracy, following the same procedure described in Section 4.3 in the case of the Cornwell index. The 'damaged' and 'intact' populations are made of $N_{rnd} = 2500$ samples, and are generated by contaminating the exact mode shapes with the Gaussian noise experimentally identified (see Fig. 21). The curves relative to TPR, FPR, and the distance of the ROC from the random classifier (proportional to the Accuracy) are plotted with respect to the threshold θ in Figs. 28(a)–28(c). The choice of the best threshold is straightforward for damage scenario R0-A1, because the maximum accuracy is well identified with the value $\theta_{opt} = 1$. For scenario $A1 - A2$, there is more overlap, and the optimal θ threshold shifts to $\theta_{opt} = 0.65$. For the damage scenario with the lowest stiffness reduction, the threshold value decreased further to $\theta_{opt} = 0.5$. However, because the TPR and FPR curves overlap in this case, different criteria can be adopted depending on the SHM targets.

In Table 6, the average numbers of TP, FN, FP and TN are calculated with respect to the optimal threshold values along with the resulting Accuracy. For a single damage position $j_d = 14$, Accuracy increases as the damage severity increases. For scenarios R0-B1 and A1-B1, with $j_d = \{4, 14\}$, two thresholds are considered separately, each relative to the specific damage case. It is worth noting that in this case, the (slightly) more challenging scenario A1-B1 also has a higher Accuracy with respect to R0-B1. In the column marked as damage-side elements (DSE), the elements found to be damaged because of DPS (see Section 4.3) are reported. Consequently, the following Accuracy+ is defined as:

$$ACC+ = \frac{TP + DSE + TN}{N} \qquad (29)$$

and its value is reported in the last column.

Table 7

True and predicted values of stiffness reduction $\beta^*_{\text{idx},j}$ on the damaged element(s) (FF BCs). The first value refers to element E_4, the second to element E_{14}.

Scenario	True values	Cornwell	Stubbs	Choi	Kim
R0-A1	–/0.91	–/0.91	–/0.99	–/0.96	–/1.04
A1-A2	–/0.86	–/0.68	–/0.97	–/0.92	–/0.95
R0-A2	–/0.81	–/0.62	–/0.97	–/0.89	–/0.99
R0-B1	0.91/0.81	0.99/0.67	0.99/0.98	0.99/0.90	1.44/1.24

(a) Scenario R0-A1.   (b) Scenario R0-A2.
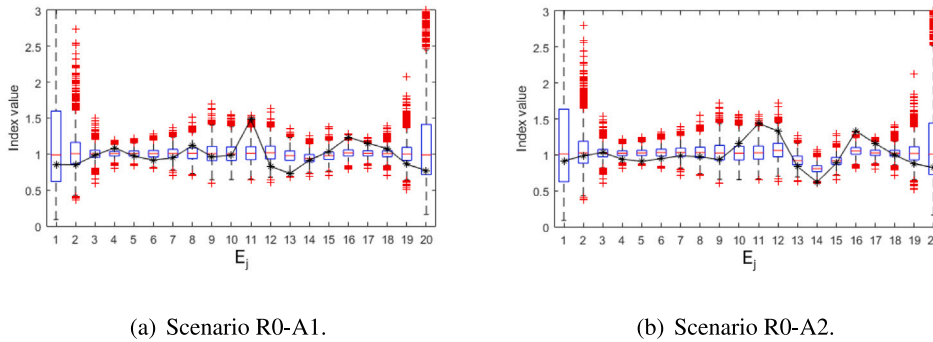
Fig. 29. Cornwell index uncertainty prediction using the experimentally identified noise under FF BCs. The coordinate x expressed in m is relative to the element mid-point $\bar{x}_j$.

5.3.2. Uncertainty in estimating severity

After localizing the damage, its severity is predicted using non-normalized indices $\beta_{\text{idx},j}$, which are directly linked to the stiffness ratio at the points where the damage is predicted. The results of the estimation of damage severity are summarized in Table 7 and are compared with the element-weighted stiffness ratio reported in the second column. It is worth noting that, as shown in the error-free condition by Dessi et al. [13], all these methods have some intrinsic limitations in predicting the correct value of stiffness reduction because of the hypotheses upon which they are developed. The Accuracy in predicting true stiffness values are more or less accurately predicted depending on the method. However, each method is sensitive to an increase in the stiffness reduction with the unique exception of the Kim and Stubbs index, which also fails to indicate the stiffness reduction in the case of small damage (scenarios R0-A1 and R0-B1). In the latter case, uncertainties related to small modal frequency variations play an important role. In terms of absolute values, because of adding unity at both the numerator and denominator, the methods of Stubbs et al. and Choi et al. generally underestimate the reduction. In contrast, Cornwell's method tends to overestimate the reduction as damage increases, but its predictions appear more precise in general.

By applying the same Monte Carlo procedure followed to estimate the optimal threshold, the uncertainty related to the damage estimation is calculated. The Cornwell index $\beta_{Co,j}$ provides the definition intrinsically more related to the stiffness reduction. For both the damage scenarios R0-A1 and R0-A2, displayed in Fig. 29, about half of the values of the experimental index fall in the 25%–75% percentile around the damage location. Oscillations in the spatial distribution due to the presence of damage move the index outside the most likely range instead. It is also worth to note that a greater uncertainty in the index value is predicted at the beam edges. The Choi index in Fig. 30 remains mostly between outliers, and shows less possibility for large deviations from unity at the beam ends. However, in the scenario R0-A2, also the Choi index value falls outside the minimum outlier in the damaged element.

5.4. Simply-supported boundary conditions

5.4.1. Damage existence and location

Simply supported BCs may experience an issue related to test repeatability, each time the beam is dismounted in the laboratory. Fixing displacements at the beam edges may slightly constrain the slopes, which is equivalent to the application of a rotational spring whose coefficient may vary depending on the specific assembly. This uncertainty might have an impact on the natural frequency of the beam, as shown in Table 8. The frequency decrease with stiffness reduction is generally monotonic. The unique exception relates to the natural frequencies of 4-th and 5-th modes for the final damage case B2, which shows the opposite trend. After spatial differentiation, low-order curvature modes exhibit a level of irregularity comparable to that of free-free BCs tests (see Fig. 31). This is not true for the first mode, which appears to be significantly more affected by the noise.

In Figs. 32–34 the normalized indices and the agreement bars are shown with reference to the damage scenarios R0-A1, R0-A2 and A1-A2, featured by different stiffness reductions on the element $j_d = 14$. In general, there is a loss of the usual Accuracy in
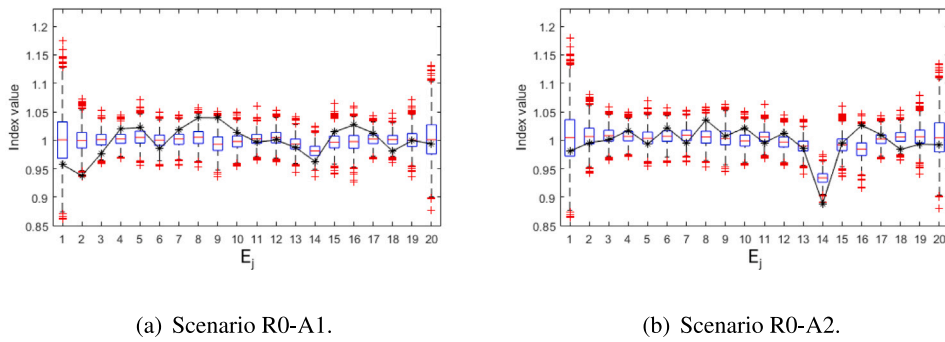
(a) Scenario R0-A1.

(b) Scenario R0-A2.

Fig. 30. Choi index uncertainty prediction using experimentally identified noise under FF BCs. The coordinate x expressed in m is relative to the element mid-point $\bar{x}_j$.
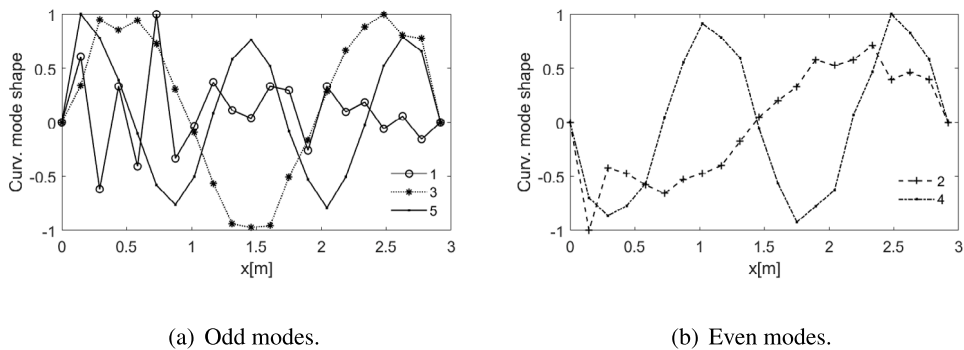

(a) Odd modes.

(b) Even modes.

Fig. 31. Curvature mode shapes for configuration R0 with simply-supported BCs.

Table 8
Frequency related to the identified vibration modes relative to different configurations for SS BCs.

Damage case	1st mode [Hz]	2nd mode [Hz]	3rd mode [Hz]	4th mode [Hz]	5th mode [Hz]
R0	15.11	57.36	131.85	229.93	347.23
A1	15.10	57.25	131.17	228.91	341.12
A2	14.94	56.78	132.48	226.80	349.04
B1	14.81	56.14	130.00	223.30	337.08
B2	14.78	55.91	129.29	223.91	343.00

damage localization (see Table 9) as the stiffness reduction becomes less significant and partially recovers if the DPS is taken into account in ACC+ (last column). It is worth noting what happens relative to scenario A1-A2 shown in Fig. 34. The Kim and Stubbs method leads to erroneous suppression of one TP and one FP, the latter being a DSE case, thus affecting both methods in evaluating the Accuracy. Thus, in Table 9, the identification results without considering the Kim and Stubbs predictions are reported, showing better results (see the row marked as A1-A2* in Table 9). This is likely to be related to the inaccuracy in reproducing the same BCs as outlined before, which directly impacts the frequency variations employed in the Kim and Stubbs index. If damage is considered also in the element E_4 (case B2, see Fig. 35), damage is correctly identified on elements E_4 and E_{14}, but some false positives not related to DPS occurrence appear on elements E_7 and E_{19}.

5.4.2. Uncertainty in estimating severity

In Table 10 the evaluation of the element-weighted stiffness ratio follows the expected trend as the damage intensity increases. The unique exception is related to the Kim and Stubbs index under scenario R0-B2. The Cornwell index overestimates the stiffness reduction again, as opposed to the Stubbs and Choi indices. The Kim and Stubbs index has alternate behavior.

The Monte Carlo method is applied again to evaluate the expected uncertainty in the prediction of the stiffness ratio after the damage. As shown in Fig. 36, there are large deviations from unit of the Cornwell index $\beta_{\mathrm{Co},j}$ also far from damaged elements, being sometimes close to the outliers. This trend is also present to a lower extent for the Choi index (Fig. 37), especially for the damage scenario R0-A2. The previous considerations suggest that the uncertainty in applying the SS BCs is responsible for this,

Table 9

True and predicted values of stiffness reduction $\beta^*_{\text{idx},j}$ on the damaged element(s) (SS BCs). In case of two-point damage, the first threshold is applied to damage in position $j = 14$, the second to position $j = 4$. The lowest of the two threshold is applied for all the other points.

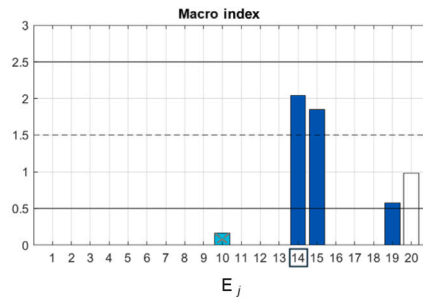| Scenario	θ_{opt}	TP	FN	FP	TN	ACC	DSE	ACC+
R0-A1	0.5	1	0	1	16	94.4%	0	94.4%
A1-A2	0.585	0	1	1	16	88.8%	1	94.4%
A1-A2*	0.585	1	0	1	16	94.4%	1	100.0%
R0-A2	1.025	1	0	1	16	94.4%	1	100.0%
R0-B1	1/0.5	1	1	3	14	77.7%	1	83.3%
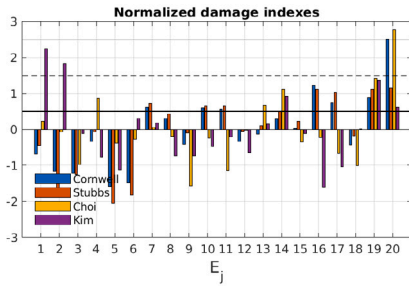
(a) All indices.
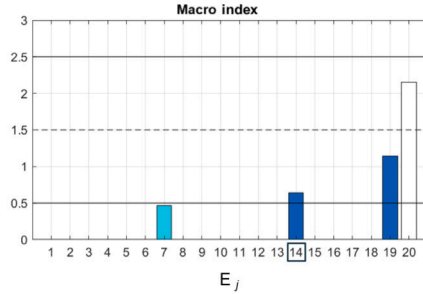
(b) Macro index evaluation.

Fig. 32. Normalized damage indices for scenario R0(intact)-A1(damaged) under SS BCs. Element-weighted stiffness ratio is $\bar{D}^*_{14} = 0.907$.
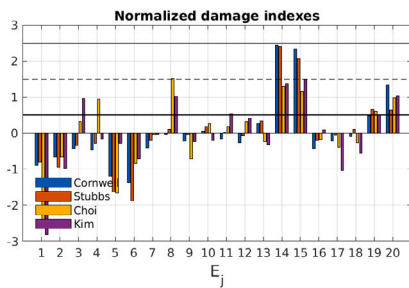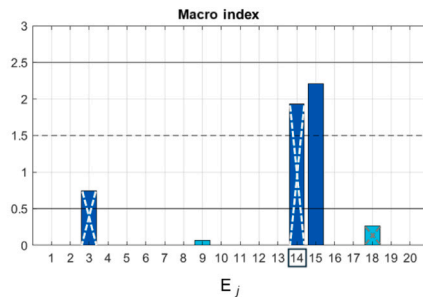

(a) All indices.

(b) Macro index evaluation.

Fig. 33. Normalized damage indices for scenario R0(intact)-A2(damaged) under SS BCs. Element-weighted stiffness ratio is $\bar{D}^*_{14} = 0.841$.
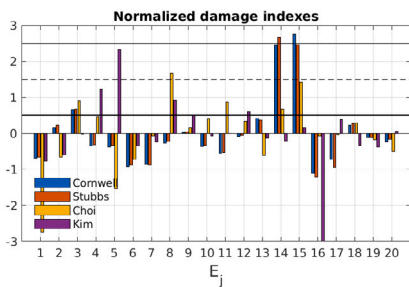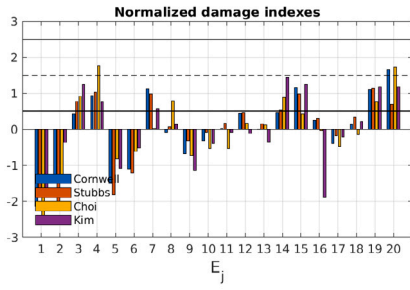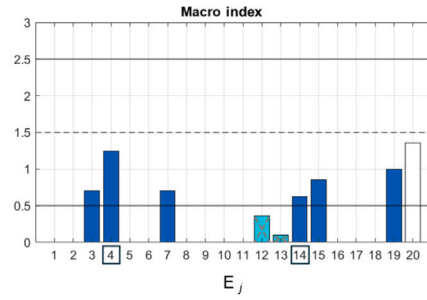

(a) All indices.

(b) Macro index evaluation.

Fig. 34. Normalized damage indices for scenario A1(intact)-A2(damaged) under SS BCs. Element-weighted stiffness ratio is $\bar{D}^*_{14} = 0.86$.

(a) All indices.

(b) Macro index evaluation.

Fig. 35. Normalized damage indices for scenario R0(intact)-B2(damaged) under SS BCs. Element-weighted stiffness ratios are $\bar{D}^*_{14} = 0.841$ and $\bar{D}^*_{04} = 0.841$.
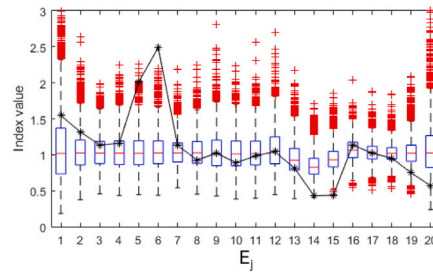
Table 10
True and predicted values of stiffness reduction $\beta^*_{\text{idx},j}$ on the damaged element(s) (SS BCs). The first value refers to element E_4, the second to element E_{14}.

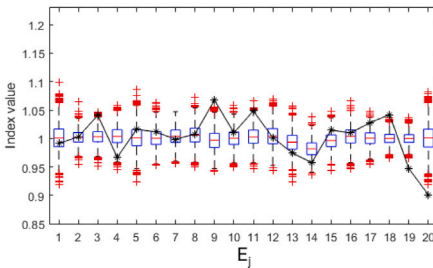| Scenario	True values	Cornwell	Stubbs	Choi	Kim
R0-A1	–/0.91	–/0.84	–/0.99	–/0.96	–/1.28
A1-A2	–/0.86	–/0.52	–/0.95	–/0.95	–/0.50
R0-A2	–/0.81	–/0.43	–/0.95	–/0.92	–/0.76
R0-B2	0.81/0.81	0.73/0.82	0.98/0.99	0.87/0.93	1.40/1.23
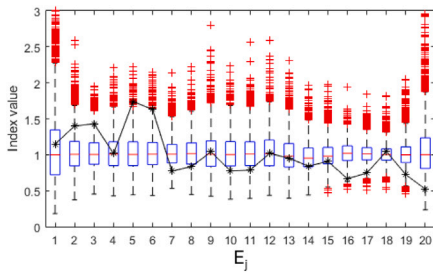
(a) Scenario R0-A1.

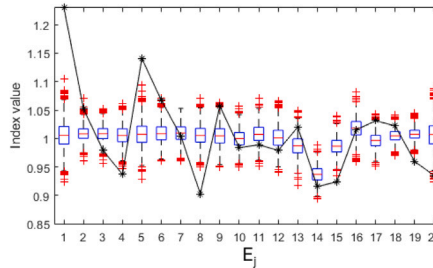(b) Scenario R0-A2.

Fig. 36. Cornwell index uncertainty prediction using experimentally identified noise under SS BCs.

(a) Scenario R0-A1.

(b) Scenario R0-A2.

Fig. 37. Choi index uncertainty prediction using experimentally identified noise under SS BCs.

as highlighted previously, because ideal BCs are considered in the perturbed analytical modal solution used for the Monte Carlo simulation.

6. Conclusions

6.1. Remarks on the developed analysis

The aim of this paper is to guide analysts in understanding and managing the uncertainties related to the analysis of structural damage using methods based on the experimental identification of modal curvatures. This objective is carried out through several steps: (*i*) the extensive analysis of error sources, (*ii*) the evaluation of uncertainties in damage localization and severity estimation using Monte Carlo simulations on synthetic data, (*iii*) the mitigation of uncertainty in damage localization using a two-stage approach based on multiple hypothesis testing and macro-index definition, and (*iv*) the introduction of optimal damage index thresholds tailored to the experimental noise levels and on the SHM goals.

The modeling of damage as a local and uniform stiffness reduction has some advantages in terms of its simply description (side thickness reduction and length), easy realization by milling and availability of analytical beam solutions which allows us to perform both sensitivity analyses and Monte Carlo simulations in a much faster way. More complex damage cases, modeled using FEM, can be considered as well at the unique cost of larger computational efforts. Curvature based methods are more suited to highlight local variation of stiffness than continuously distributed or uniform damage. Nonetheless, it has been theoretically demonstrated that these methods can identify distinct damage locations if damage occurs in elements separated at least by two non-damaged elements. It is worth noting that the methods based only on the curvature analysis suppose negligible mass variation due to damage in its definition, which is in general fully satisfied if damage is generated with a sharp cut.

A crucial aspect in designing the sensor layout for damage identification is the type and number of measurement points. To be sensitive to curvature and stiffness variations between measurement nodes, curvatures calculated from displacement modes with finite differences are recommended. The optimal distance h between sensors is found to be a compromise between opposite trends relative to truncation and bias errors affecting the calculation of the curvature integrals. A conservative estimate of this optimal distance, minimizing the error in the strain–energy integrals, has been analytically provided for free-free and simply supported BCs, but it can be easily extended to other cases.

Another important aspect addressed in this study is the reliability of damage predictions. In this respect, it has been highlighted that the numerical procedure for the index calculations necessarily causes a so-called Damage Position Spill, such as the side elements of the damaged one appearing positive after testing. This evidence should be considered when evaluating the performance of the employed techniques. For this reason, a different accuracy calculation is also introduced, which considers the Damage Spilled Elements not as False Positives but as True Positives because the error is about position and not on damage existence. The main factor affecting the daily reliability of the experimental identification of damage is related to the uncertainty in the input data, that is, the set of displacement modes. It has been shown in laboratory tests that this uncertainty is also related to the type of BCs, which means that the measurement noise relative to the same sensor layout may affect the identification procedure in a different way. Moreover, relative to tests with SS BC, the small changes in the BCs each time the experimental setup is restored after damage milling have a negative impact on accuracy, which is lower with respect to FF BCs.

6.2. Extension to real cases

These concepts have important implications for real-world structures. First, the noise in the vibration mode shapes must be periodically verified. Second, changes in the BCs may induce errors in damage identification analysis. Focusing on structures with geometric BCs (e.g., simply supported, clamped, or fixed with springs), BCs are simply an idealization of the elastic link provided by the structural domain outside the monitored one. For instance, the occurrence of structural modifications outside the observed substructures or temperature variations consistently affects the effectiveness of some damage identification techniques, requires specific treatment (see *e.g.*, [29]), and must be monitored carefully. Techniques based on virtual sensing, such as those mentioned in the introduction, may play a role in this task. Nevertheless, it is worth underlining that the present tests might be more challenging from a certain point of view than real situations, despite the simplicity of the analyzed structure. Output-only analysis, for instance, provides less noisy modes than the RHT technique because of the longer acquisition and greater averaging of the identified modes.

The main mitigation of uncertainty in real conditions is provided by the definition of the macro-index for damage localization, which involves separately the indices under the so-called agreement condition and their combination under their averaging. This procedure is effective in avoiding false positives at the agreement level and allows for lowering the threshold applied to the macro-index, thus minimizing false negatives. Moreover, the threshold is set on the basis of a hybrid approach, which simulates the experimental noise propagation up to the damage indices and allows for deciding the best threshold that separates the intact and damaged classes more efficiently. Finding the best compromise becomes more difficult as the noise level on the data increases, making the choice of the threshold more linked to follow either minimization of FP or maximization of TP. It has been shown that the optimal threshold, at least for the considered structure, does not depend significantly on the position. However, its definition requires some parametrization of the damage severity one may expect, or using as first guess the information provided by the damage analysis. An important value of the developed uncertainty analysis is in the possibility to 'a priori' estimate, based on the ascertained noise conditions, which is the smallest damage one can precisely locate or, alternatively, what threshold or noise levels on data best suits the SHM objectives. A critical aspect may be the availability of accurate or updated numerical models, as previously explained. Therefore, during condition monitoring of the structure, model updating of the reference structure, which is assumed to be damage-free, must be performed.

The extension of the developed analysis concepts to complex structures is rather straightforward for 1D slender structures or plates. However, there is much work ahead to demonstrate the usefulness and adapt the theory to structures where damage may occur in elements of different natures, such as stiffened plates or bridges (see *e.g.*, [30,31]).

CRediT authorship contribution statement

Daniele Dessi: Writing – original draft, Supervision, Software, Methodology, Conceptualization, Writing – review & editing. **Fabio Passacantilli:** Data curation, Investigation, Writing – review & editing. **Andrea Venturi:** Conceptualization, Investigation, Writing – review & editing.

Declaration of competing interest

The authors declare that they have no known competing financial interests or personal relationships that could have appeared to influence the work reported in this paper.

Acknowledgments

Data availability

Data will be made available on request.

References

[1] Z. Deng, M. Huang, N. Wan, J. Zhang, The current development of structural health monitoring for bridges: A review, Buildings 13 (2023) 1360, http://dx.doi.org/10.3390/buildings13061360.

[2] A. Pandey, M. Biswas, M. Samman, Damage detection from changes in curvature mode shapes, J. Sound Vib. 145 (2) (1991) 321–332, http://dx.doi.org/10.1016/0022-460X(91)90595-B.

[3] C. Ratcliffe, Damage detection using a modified Laplacian operator on mode shape data, J. Sound Vib. 204 (3) (1997) 505–517, http://dx.doi.org/10.1006/jsvi.1997.0961.

[4] N. Stubbs, J.-T. Kim, C.R. Farrar, Field verification of a nondestructive damage localization and severity estimation algorithm, in: Proceedings of the 13th International Modal Analysis Conference, Nashville, Tennessee, 1995, pp. 210–218.

[5] P. Cornwell, S. Doebling, C. Farrar, Application of strain energy damage detection method to plate-like structures, J. Sound Vib. 224 (2) (1999) 359–374, http://dx.doi.org/10.1006/jsvi.1999.2163.

[6] S. Choi, S. Park, N. Stubbs, Nondestructive damage detection in structures using changes in compliance, Int. J. Solids Struct. 42 (15) (2005) 4494–4513, http://dx.doi.org/10.1016/j.ijsolstr.2004.12.017.

[7] S. Choi, S. Park, S. Yoon, N. Stubbs, Nondestructive damage identification in plate structures using changes in modal compliance, NDT E Int. 38 (7) (2005) 529–540, http://dx.doi.org/10.1016/j.ndteint.2005.01.007.

[8] J. Kim, N. Stubbs, Improved damage identification method based on modal information, J. Sound Vib. 252 (2) (2002) 223–238, http://dx.doi.org/10.1006/jsvi.2001.3749.

[9] W. Fan, P. Qiao, A strain energy-based damage severity correction factor method for damage identification in plate-type structures, Mech. Syst. Signal Process. 28 (2012) 210–218, http://dx.doi.org/10.1016/j.ymssp.2011.11.010.

[10] N. Stubbs, S. Park, C. Sikorsky, S. Choi, A global non-destructive damage assessment methodology for civil engineering structures, Int. J. Syst. Sci. 31 (11) (2010) 1361–1373, http://dx.doi.org/10.1080/00207720050197758.

[11] A. Rytter, Vibration based inspection of civil engineering structures, in: Doctoral Dissertation, Department of Building Technology and Structural Engineering, University of Aalborg, Denmark, 1993.

[12] G. Garcia, K. Butler, N. Stubbs, Relative performance of clustering-based neural network and statistical pattern recognition models for nondestructive damage detection, Smart Mater. Struct. 6 (4) (1997) 415–424, http://dx.doi.org/10.1088/0964-1726/6/4/005.

[13] D. Dessi, G. Camerlengo, Damage identification techniques via modal curvature analysis: Overview and comparison, Mech. Syst. Signal Process. 52–53 (1) (2015) 181–205, http://dx.doi.org/10.1016/j.ymssp.2014.05.031.

[14] C. Farrar, D. Jauregui, Damage detection algorithms applied to experimental and numerical modal data from the i-40 bridge, Los Alamos National Laboratory Technical Report, LA-13074-MS, 1996, pp. 210–218.

[15] J. Zhang, M. Huang, N. Wan, Z. Deng, Z. Ye, Missing measurement data recovery methods in structural health monitoring: The state, challenges and case studies, Measurement 231 (2024) 114528, http://dx.doi.org/10.1016/j.measurement.2024.114528.

[16] F. Saltari, D. Dessi, F. Mastroddi, Mechanical systems virtual sensing by proportional observer and multi-resolution analysis, Mech. Syst. Signal Process. 146 (2021) 107003, http://dx.doi.org/10.1016/j.ymssp.2020.107003.

[17] E. Reynders, R. Pintelon, G.D. Roeck, Uncertainty bounds on modal parameters obtained from stochastic subspace identification, Mech. Syst. Signal Process. 28 (2008) 948–969, http://dx.doi.org/10.1016/j.ymssp.2007.10.009.

[18] E. Reynders, K. Maes, G. lombaertn, G.D. Roeck, Uncertainty quantification in operational modal analysis with stochastic subspace identification: Validation and applications, Mech. Syst. Signal Process. 66–67 (2016) 13–30, http://dx.doi.org/10.1016/j.ymssp.2015.04.018.

[19] S. Gres, M. Dohler, L. Mevel, Uncertainty quantification of the modal assurance criterion in operational modal analysis, Mech. Syst. Signal Process. 152 (2021) 107457, http://dx.doi.org/10.1016/j.ymssp.2020.107457.

[20] Y. Zhang, J. Guo, Y. Xie, J. Xu, Warship damage identification using mode curvature shapes method, Appl. Ocean Res. 152 (2022) 103396, http://dx.doi.org/10.1016/j.apor.2022.103396.

[21] E. Erduran, F. Ulla, L. Naess, A framework for long-term vibration-based monitoring of bridges, Sensors 21 (14) (2021) 4739, http://dx.doi.org/10.3390/s21144739.

[22] S. Park, N. Stubbs, R. Bolton, S. Choi, C. Sikorsky, Field verification of the damage index method in a concrete box-girder bridge via visual inspection, Comput. Aided Civ. Infrastruct. Eng. 16 (2001) 58–70, http://dx.doi.org/10.1006/jsvi.2001.3749.

[23] S. Choi, N. Stubbs, Damage identification in structures using the time-domain response, J. Sound Vib. 275 (2004) 577–590, http://dx.doi.org/10.1016/j.jsv.2003.06.010.

[24] F.B. Hildebrand, Introduction To Numerical Analysis, Dover Publications Inc., 1974.

[25] P.M. Prenter, Splines and Variational Methods, John Wiley & Sons, 1989.

[26] L. Meirovitch, Fundamentals of Vibrations, McGraw-Hill, 2001.

[27] W. Fan, P. Qiao, Vibration-based damage identification methods: A review and comparative study, Struct. Health Monit. 10 (1) (2011) 83–111, http://dx.doi.org/10.1177/1475921710365419.

[28] S. Choi, S. Park, N.-H. Park, N. Stubbs, Improved fault quantification for a plate structure, NDT E Int. 297 (2006) 865–879, http://dx.doi.org/10.1016/j.jsv.2006.05.002.

[29] M. Huang, J. Zhang, J. Hu, Z. Ye, Z. Deng, N. Wan, Nonlinear modeling of temperature-induced bearing displacement of a long-span single-pier rigid frame bridge based on DCNN-LSTM, Case Stud. Therm. Eng. 53 (2024) 103897, http://dx.doi.org/10.1016/j.csite.2023.103897.

[30] D. Wadadar, D.D. Mandal, S. Banerjee, Performance of vibration based damage detection algorithms for detection of disbond in stiffened metallic plates, Procedia Eng. 144 (2016) 242–252, http://dx.doi.org/10.1016/j.proeng.2016.05.030.

[31] M. Huang, Z. Ling, C. Sun, Y. Lei, C. Xiang, Z. Wan, J. Gu, Two-stage damage identification for bridge bearings based on sailfish optimization and element relative modal strain energy, Struct. Eng. Mech. 86 (6) (2023) 715–730, http://dx.doi.org/10.12989/sem.2023.86.6.715.